Bioactive Materials 48 (2025) 510–528

Contents lists available at ScienceDirect

Bioactive Materials

journal homepage: www.keaipublishing.com/en/journals/bioactive-materials

Multifunctional magneto-electric and exosome-loaded hydrogel enhances neuronal differentiation and immunoregulation through remote non-invasive electrical stimulation for neurological recovery after spinal cord injury

Wubo Liu [a,b,c,d,e,f], Qiang Liu [h], Zeqin Li [b,d,e,f,m], Chunjia Zhang [b,d,e,f,g,i], Zehui Li [b,d,e,f,g], Han Ke [a,b,c,d,e,f,l], Xin Xu [a,b,d,e,f,g], Xiaoxin Wang [b,d,e,f,g], Huayong Du [b,d,e,f,g], Zuliyaer Talifu [b,c,d,e,f,g,j], Yunzhu Pan [b,c,d,e,f,g,k], Xiaoxiong Wang [a,c], Jingyun Mao [n], Feng Gao [b,d,e,f,g], Degang Yang [b,d,e,f,g], Yan Yu [b,d,e,f,g], Xinyu Liu [a,c,*], Jianjun Li [a,b,c,d,e,f,g,**]

[a] Department of Orthopaedics, Qilu Hospital, Cheeloo College of Medicine, Shandong University, Jinan, Shandong, 250012, PR China
[b] China Rehabilitation Research Center, Beijing Bo'ai Hospital, Beijing, 100068, PR China
[c] University of Health and Rehabilitation Sciences, Qingdao, Shandong, 266100, PR China
[d] China Rehabilitation Science Institute, Beijing, 100068, PR China
[e] Beijing Key Laboratory of Neural Injury and Rehabilitation, Beijing, 100068, PR China
[f] Center of Neural Injury and Repair, Beijing Institute for Brain Disorders, Beijing, 100068, PR China
[g] School of Rehabilitation, Capital Medical University, Beijing, 100069, PR China
[h] Department of General Surgery, The First Affiliated Hospital of Nanchang University, Nanchang, Jiangxi, 330006, PR China
[i] Department of Rehabilitation Medicine, Peking University Third Hospital, Beijing, 100096, PR China
[j] School of Population Medicine and Public Health, Chinese Academy of Medical Sciences/Peking Union Medical College, Beijing, 100005, PR China
[k] Rehabilitation Department, Beijing Hospital, National Center of Gerontology, Institute of Geriatric Medicine, Chinese Academy of Medical Sciences, 100005, PR China
[l] Department of Orthopedics, Beijing Chaoyang Hospital, Capital Medical University, Beijing, 100013, PR China
[m] Ganan Medical University, Ganzhou, Jiangxi, 341000, PR China
[n] College of Environmental and Resource Sciences, College of Carbon Neutral Modern Industry, Fujian Normal University, Fuzhou, 350007, PR China

ARTICLE INFO

Keywords:
Spinal cord injury repair
Tissue engineering
Magneto-electric nanoparticles
HUMSC-Exos
Neuronal differentiation

ABSTRACT

Intervention in the differentiation of neural stem cells (NSCs) is emerging as a highly promising approach for the treatment of spinal cord injury (SCI). However, NSCs at the injury site often suffer from low survival and uncontrolled differentiation. Whereas electrical stimulation has proven effective in regulating the fate of NSCs and promoting tissue repair, however, conventional electrical stimulation therapy has failed to be widely applied due to challenges such as invasiveness and technical complexity. To overcome these limitations, we developed a biomimetic magneto-electric hydrogel incorporating Fe_3O_4@$BaTiO_3$ core-shell nanoparticles and human umbilical mesenchymal stem cell exosomes (HUMSC-Exos) around the concept of constructing remote noninvasive electrical stimulation for the synergistic treatment of SCI. The Fe_3O_4@$BaTiO_3$ is activated by the peripheral magnetic field to generate electrical stimulation, which, in conjunction with the synergistic effects of HUMSC-Exos, significantly alleviates the early inflammatory response associated with SCI and enhances the regeneration of newborn neurons and axons, thereby creating favorable conditions for functional recovery post-SCI. Our findings indicate that applying this magneto-exosome hydrogel in a rat model of SCI leads to substantial functional recovery. This innovative combination represents a promising therapeutic strategy for SCI repair.

Peer review under the responsibility of KeAi Communications Co., Ltd.
* Corresponding author. Department of Orthopaedics, Qilu Hospital, Cheeloo College of Medicine, Shandong University, Jinan, Shandong, 250012, PR China.
** Corresponding author. China Rehabilitation Research Center, Beijing Bo'ai Hospital, Beijing, 100068, P.R. China.
E-mail addresses: newyuliu@163.com (X. Liu), 13718331416@163.com (J. Li).

https://doi.org/10.1016/j.bioactmat.2025.02.034
Received 31 October 2024; Received in revised form 22 February 2025; Accepted 23 February 2025

1. Introduction

Spinal cord injury (SCI) is a severe and debilitating condition, and its incidence has been rising in recent years due to traffic accidents, workplace incidents, and sports-related injuries [1,2]. These injuries can significantly impair the sensory, motor, and autonomic functions of patients [3], resulting in substantial economic burdens for them, their families, and society as a whole [4]. Recently, intervention with neural stem cells (NSCs) have emerged as a promising approach for treating SCI, as NSCs have the potential to differentiate into functional neurons, rebuild neural circuits, and promote nerve regeneration [5,6]. However, NSCs at the site of injury often suffer from low survival and uncontrolled differentiation [7]. These issues arise from the inflammatory microenvironment created by immune cell activation and the release of inflammatory factors at the injury site, which hinders neural growth [8]. In this environment, endogenous NSCs are more likely to differentiate into glial cells rather than neurons [9]. Furthermore, patients with spinal cord injuries experience disruption of nerve fiber conduction and limited spontaneous axonal regeneration at the injury sites. This disruption impairs neuroelectric signaling, which further restricts essential processes such as neuronal growth, survival, and expression [10–12].

Electrical stimulation has been demonstrated in previous research to influence the fate of NSCs [13,14] and facilitate the repair of damaged tissues, including nerves, bones, and muscles [15,16]. Functional electrical stimulation plays a crucial role in the treatment of SCI by promoting partial recovery of standing and walking abilities [17–19]. However, traditional methods of electrical stimulation require the surgical implantation of electrodes, which can increase the risk of infection and necessitate subsequent surgeries for electrode removal [20,21]. With the anticipated increase in the aging population and the rising incidence of SCI patients, there is an urgent need for improved methods of electrical stimulation. Non-invasive remote wireless electrical stimulation technology offers new insights for the treatment of SCI [22]. Compared to conventional electrical stimulation, remote wireless electrical stimulation demonstrates significant advantages in the treatment of SCI, as it can convert external field energy into electrical signals, thereby enabling non-invasive stimulation [23,24]. Wireless electrical stimulation avoids the surgical risks and complications associated with implanted electrodes, such as infection and inflammation, while minimizing the need for additional surgeries for patients [25,26]. This innovative technology overcomes the physical limitations of conventional electrical stimulation, offering a safer and more effective therapeutic option for patients with SCI, and holds significant promise for broad clinical applications.

In recent years, piezoelectric materials have been explored for electrode-free external biosafety electrical stimulation due to their ability to convert mechanical energy into electrical energy [27,28]. Most studies have focused on triggering the piezoelectric response through either external stress or ultrasonic stimulation. Direct stress stimulation is typically applied to skeletal areas, while ultrasonic stimulation can generate heat and cavitation effects, which may harm neural tissue [29–31]. Consequently, there is a need for a novel piezoelectric excitation method that effectively supports nerve recovery following SCI.

Magneto-electric materials that utilize a mild magnetic field as an external stimulation source to generate piezoelectric output can address the challenges associated with traditional methods. Polyvinylidene fluoride (PVDF) has garnered significant attention in biomedicine due to its favorable piezoelectric properties [32–34]. However, its limited biocompatibility and in vivo degradation hinder its use in neural tissue repair. In contrast, barium titanate ($BaTiO_3$) offers excellent piezoelectric properties along with improved biocompatibility [33]. $BaTiO_3$ has been extensively used in bone tissue regeneration [35–37], yet there is limited research on the combined effects of $BaTiO_3$ and Fe_3O_4 in nerve repair, particularly in the context of SCI. This study aims to explore the role of Fe_3O_4@$BaTiO_3$ nanoparticles as radio-stimulators in the regeneration process following SCI.

Hydrogels are widely used in promoting cell growth and tissue formation after SCI due to their soft, hydrated structure that closely resembles natural neural tissue. They provide a three-dimensional environment conducive to the efficient transmission of electrical signals [38–40]. In our study, a hydrogel consisting of gelatin, a collagen degradation product, with methacrylate (GelMA) was used to load Fe_3O_4@$BaTiO_3$, providing excellent scaffolding material for SCI repair. This GelMA 3D hydrogel system exhibits properties akin to those of neural tissues, including high permeability to oxygen and nutrients, high water content, and moderate mechanical strength. These characteristics create an optimal environment for cell growth and support SCI repair [41].

Given the harmful inflammatory microenvironment following SCI and the potential inflammatory response triggered by the implantation of biomaterials [42], incorporating an anti-inflammatory component into the hydrogel is essential. Human umbilical cord mesenchymal stem cells (HUMSCs) are particularly valuable in therapeutic interventions due to their remarkable proliferative capacity and low immunogenicity [43,44]. The exosomes secreted by HUMSCs (HUMSC-Exos) are rich in mRNAs, miRNAs, growth factors, and proteins, which makes them effective modulators of inflammation [45,46]. By delivering these immunomodulatory HUMSC-Exos within hydrogels, we can reduce adverse host responses and enhance the hydrogels' ability to promote functional recovery.

Therefore, we developed a composite hydrogel composed of Fe_3O_4@$BaTiO_3$, HUMSC-Exos, and GelMA, featuring anti-inflammatory properties and wireless piezoelectricity for SCI regeneration (Scheme 1). The process began with the synthesis of Fe_3O_4 nanoparticles, followed by the formation of a $BaTiO_3$ nanoparticle layer on their surface. Subsequently, we synthesized GelMA hydrogel (GM) from gelatin and methacrylate, which closely resembles the composition, viscoelasticity, low modulus, and fiber structure of neural extracellular matrix (ECM). Next, we immobilized HUMSC-Exos and Fe_3O_4@$BaTiO_3$ within the GelMA hydrogel network, resulting in the creation of a GelMA-magneto-electric nanoparticles-exosomes hydrogel (GMNPE). We then evaluated the magneto-electric properties, anti-inflammatory effects, biocompatibility, and pro-neural differentiation capabilities of GMNPE in vitro. Additionally, we identified the specific signaling pathways through which GMNPE promotes axonal regeneration. To further assess the effectiveness of GMNPE in promoting nerve regeneration and functional recovery following SCI, we established a rat spinal cord hemisection model.

2. Materials and methods

2.1. Synthesis and characterization of Fe_3O_4@$BaTiO_3$

A total of 1.35 g of $FeCl_3{\cdot}6H_2O$ (Aladdin, Shanghai, China) and 3.6 g of CH_3COONa (Aladdin, Shanghai, China) were accurately measured and added to 72 mL of ethylene glycol. This mixture was then stirred and dispersed using ultrasonication. Subsequently, the resulting solution was transferred to a 100 mL polytetrafluoroethylene reactor and placed in a hydrothermal oven set at a constant temperature of 200 °C for 16 h. Upon completion of the reaction, the solution was allowed to cool naturally to room temperature. The product was then washed several times with deionized water and anhydrous ethanol, followed by drying under a vacuum at 40 °C to yield Fe_3O_4 nanoparticles.

Next, 0.271 g of $Ba(OH)_2{\cdot}8H_2O$ (Aladdin, Shanghai, China) and 0.672 g of KOH (Aladdin, Shanghai, China) were dissolved in 30 mL of water and subjected to ultrasonic stirring for a brief period. Meanwhile, 0.293 g of $(C_4H_9O)_4Ti$ (Aladdin, Shanghai, China) was mixed in 30 mL of n-butanol until well combined. The two solutions were then mixed together, and 0.1 g of Fe_3O_4 nanoparticles, prepared in the previous step, was added to the mixture. After stirring for a designated time, the combined solution was transferred to a 100 mL polytetrafluoroethylene

reactor and placed in a water-heated air blower set to 180 °C. Once the reaction was complete, the solution was allowed to cool to room temperature naturally. The resulting product was washed several times with deionized water and anhydrous ethanol, then dried under vacuum at 40 °C to yield Fe_3O_4@$BaTiO_3$ nanoparticles.

The morphology of Fe_3O_4 and Fe_3O_4@$BaTiO_3$ nanoparticles was analyzed using scanning electron microscopy (SEM, ZEISS Gemini 300, Germany) and transmission electron microscopy (TEM, FEI Talos F200x, USA). X-ray diffraction (XRD) analysis was conducted with a Rigaku SmartLab (Japan) over a scanning range of 5°–90° at a scanning speed of 2°/min. The particle size distribution of the nanoparticles was assessed through dynamic light scattering (DLS, Malvern Zetasizer Nano ZS90, UK). The saturation magnetization of the nanoparticles was measured using a vibrating sample magnetometer (VSM, LakeShore 7404, USA) within a magnetic field strength range of 0–20,000 Oe. Additionally, the piezoelectric response of the nanoparticles was evaluated using atomic force microscopy (AFM, Bruker Dimension Icon, Germany).

2.2. Isolation and characterization of HUMSC-Exos

HUMSC-Exos are extracellular vesicles derived from human umbilical cord mesenchymal stem cells. The exosomes are isolated from the culture supernatant using tangential flow filtration (TFF). The particle size distribution and concentration of exosomes were measured using a Flow NanoAnalyzer (NanoFCM Inc., Xiamen, China). Their morphology was visualized with transmission electron microscopy (TEM, HITACHI H-7650). Additionally, the presence of specific biomarkers in the exosomes was evaluated using Western blotting. The antibodies utilized for this analysis included CD9 (Abcam, Cambridge, UK), CD81 (CST, USA), Alix (Abcam, Cambridge, UK), and Calnexin (Proteintech, USA).

2.3. Fabrication and characterization of GMNPE hydrogels

A 10 % (w/v) gelatin solution was prepared by dissolving 1 g of gelatin powder in 10 ml of phosphate-buffered saline (PBS), which was heated to 40 °C in a water bath and stirred for 1 h. To this solution, 2.5 ml of methacrylic anhydride was added at a concentration of 0.5 ml/L and stirred at 50 °C for 3 h. The reaction was halted by adding 40 ml of PBS, after which the solution was dialyzed against deionized water, lyophilized, and set aside. Before the preparation of the GMNPE hydrogel, the prepared GelMA solution (3 % w/v) will be sterilized using a 0.22 μm sterile filter. Subsequently, varying concentrations of Fe_3O_4@$BaTiO_3$ (0, 0.5, 1, and 2 % wt), which have been sterilized by ultraviolet irradiation for 30 min, will be added and thoroughly mixed

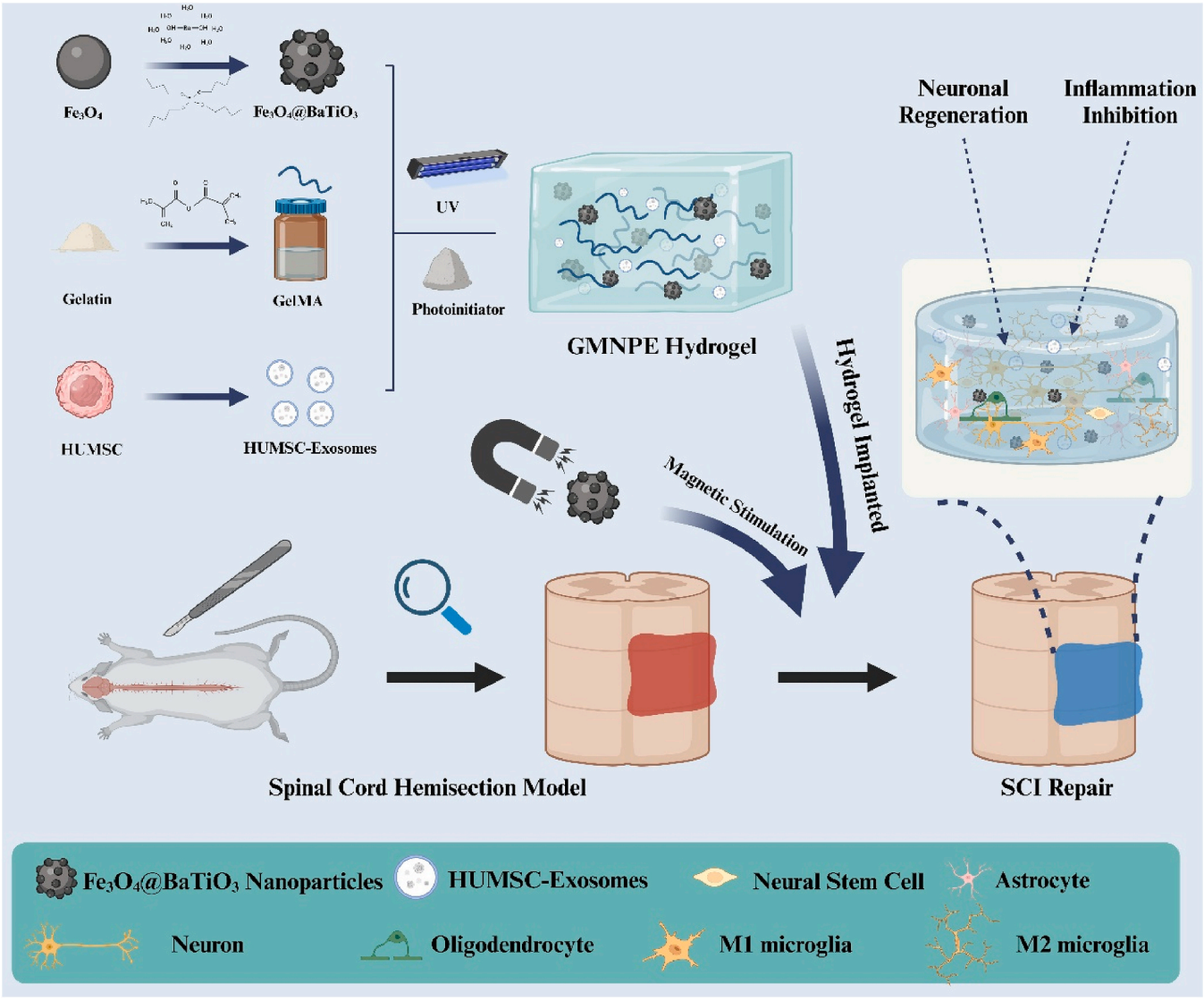

Scheme 1. Schematic illustration of the synthesis steps of GMNPE hydrogel and the promotion of neuronal regeneration after SCI as well as inflammation inhibition in the presence of a remote magnetic field.

into the GelMA solution. Following this, 200 μg of HUMSC-Exos drops were introduced into 50 μL of the aqueous gel and incubated overnight at 4 °C. The resulting hydrogel was mixed with a 10 % photoinitiator (SP-BI-C02-2, SunP, China) and subjected to UV cross-linking (3W, 405 nm) for 15 s to form the GMNPE hydrogel. GM hydrogels (without the addition of Fe_3O_4@$BaTiO_3$ and HUMSC-Exos), GME (GelMA -exosomes) hydrogels (without the addition of Fe_3O_4@$BaTiO_3$), and GMNP (GelMA-magneto-electric nanoparticles) hydrogels (without the addition of HUMSC-Exos) were synthesized using the same method described above.

The morphology of the hydrogels was analyzed using SEM (ZEISS Gemini 300, Germany). The rheological properties were assessed with a rheometer (Haake Mars40, Germany), with angular frequency varying from 1 to 100 rad/s. To evaluate the electrical stimulation intensity of GMNPE hydrogel under the influence of a magnetic field, GMNPE was solidified in a 35 mm diameter cell culture dish and subsequently placed within a Helmholtz coil (Paisheng Technology, Hunan, China). The output current of GMNPE was measured using a low-power current analyzer (LPT2020, China). For degradation analysis, GMNPE (initial weight W0) was subjected to vacuum freeze-drying at −80 °C for 24 h, followed by immersion in PBS containing 1 mg/ml lysozyme at 37 °C. Each week, the samples were retrieved, freeze-dried, and weighed (W1). The degradation extent of the hydrogel was quantified as W1/W0 × 100 %. Prior to freeze-drying, the intensity of the microcurrent generated by the samples under a magnetic field was measured to evaluate the impact of hydrogel degradation on the stability of electrical stimulation. To evaluate swelling, the hydrogels were immersed in phosphate-buffered saline (PBS) at room temperature until fully saturated. The wet weight (W_1) of each hydrogel was recorded, followed by measuring the dry weight (W_2) after vacuum lyophilization at −80 °C. The swelling ratio of the hydrogel was calculated using the following equation:

$$Swelling\ ratio(\%) = \frac{W_1 - W_2}{W_2} \times 100\% \quad (1)$$

2.4. Cell line, cell cultivation and cellular intervention

NSCs were isolated from rat embryos (E13-15) by mechanically dissociating the embryonic brain into individual cells, which were then transferred to culture flasks for suspension culture. The extracted NSCs were cultured in a specific medium composed of 47.5 ml DMEM/F12 (Gibco), 1 ml B27 neuronal supplement (Gibco), 0.5 ml N2 neuronal supplement (Gibco), 0.5 ml Glutamax (Gibco), 0.5 ml penicillin/streptomycin (Gibco), and supplemented with 20 ng/ml epidermal growth factor (EGF, MCE) and 20 ng/ml basic fibroblast growth factor (bFGF, MCE). NSCs were then seeded in culture plates containing GMNPE hydrogel. The plates were subjected to a pulsed magnetic field (15 mT, 60 Hz, 50 % duty cycle) generated by a Helmholtz coil. This stimulation was applied for 0.5 h per day over a period of 7 days, after which the cells were collected for further assays.

2.5. Exosomes labeling and cell phagocytosis studies

Exosomes were labeled using the PKH26 red fluorescent membrane linker dye (MCE). Initially, the exosomes were resuspended in 500 μL of Diluent C solution, to which 5 μL of PKH26 dye was added. The mixture was vortexed for 1 min and incubated for an additional 10 min. To neutralize any unbound dye, 10 ml of complete DMEM medium was added, and the exosomes were then centrifuged at 100,000 g for 1 h at 4 °C to wash the precipitate. To assess exosome phagocytosis, cytoskeletal staining with β-actin was performed. Cells were first fixed with 4 % paraformaldehyde for 30 min and then treated with 5 % BSA containing 0.3 % Triton X-100 (Sigma, Germany) for 1 h at room temperature. The primary antibody (β-actin, Servicebio, Wuhan, China) was added and the samples were incubated overnight at 4 °C. After washing away excess antibody with PBS, DAPI (Servicebio, China) was applied and incubated at room temperature for 10 min. Images were captured using a confocal microscope (Nikon ECLIPSE TI-S, Japan).

2.6. Biosafety and proliferation ability of hydrogels at different nanoparticles concentrations on NSCs

The survival of NSCs in hydrogels: Neurospheres were dissociated into single cells and seeded into 24-well plates containing hydrogels with varying concentrations of Fe_3O_4@$BaTiO_3$ (0, 0.5, 1, and 2 % wt). The viability of the NSCs was assessed at 1, 4, and 7 days using calcein-AM/propidium iodide (Calcein-AM/PI, Beyotime, China) staining. The stained cells were then imaged with a confocal microscope (Nikon ECLIPSE TI-S, Japan) to evaluate cell survival.

Proliferation capacity of NSCs in hydrogels: NSCs were incubated in 96-well plates containing hydrogels with varying concentrations of Fe_3O_4@$BaTiO_3$ (0, 0.5, 1, and 2 % wt). At days 1, 4, and 7, 10 % CCK-8 solution (Beyotime, China) was added to each well. After 1 h of incubation, 100 μL of the supernatant was transferred to new 96-well plates, and absorbance was measured at 450 nm using a PerkinElmer Enspire enzyme-labeling instrument (Singapore) to assess cell viability.

2.7. Gene expression

Total RNA was extracted from cells or spinal cord tissues using the Total RNA Extraction Kit (DP419, Tengen) following the manufacturer's instructions. The concentration and purity of the extracted RNA were assessed with a Nanodrop 2000 spectrophotometer (Thermo Fisher Scientific, Waltham, MA, USA). Next, individual samples were divided and diluted, and cDNA synthesis was performed using the cDNA First Strand Synthesis Kit (G3337, Servicebio, Wuhan, China). Quantitative reverse transcription-polymerase chain reaction (qRT-PCR) was conducted using the qPCR premix (G3327, Servicebio, Wuhan, China) under the following conditions: an initial denaturation at 95 °C for 10 min, followed by 40 cycles of denaturation at 95 °C for 15 s, and annealing/extension at 60 °C for 60 s. Relative mRNA expression levels were calculated using the 11CT method, with GAPDH as the reference gene. Each analysis was performed in triplicate. The primer sequences used for PCR are provided in Table S1.

2.8. RNA sequence analysis

Total RNA extracted from NSCs in the control and GMNPE + MS groups was subjected to RNA sequencing analysis at OE Biotech Co., Ltd. (Shanghai, China). Differentially expressed genes (DEGs) between the two groups were identified using a threshold of $|\log2(\text{fold change})| > 1.5$ and adjusted p-value <0.05, followed by hierarchical clustering visualization via a heatmap. Gene Ontology (GO) enrichment analysis was performed to categorize biological processes, molecular functions, and cellular components associated with the DEGs. Additionally, Kyoto Encyclopedia of Genes and Genomes (KEGG) pathway analysis was conducted to elucidate signaling pathways significantly enriched in the GMNPE + MS group compared to controls.

2.9. Immunofluorescent staining

Cells or spinal cord tissues were fixed in 4 % paraformaldehyde (PFA, Servicebio, China) for 30 min, followed by washing with PBS to remove any residual PFA. The samples were then incubated in 5 % BSA containing 0.3 % Triton X-100 (Sigma, Germany) for 1 h at room temperature. Primary antibodies were subsequently added and incubated overnight at 4 °C. After washing away the excess antibodies with PBS, the corresponding secondary antibodies were added and incubated for 1 h at room temperature, protected from light. Finally, DAPI (Servicebio, China) was added and incubated for 10 min at room temperature. Images were captured using a confocal microscope (Nikon ECLIPSE TI-S, Japan). The primary antibodies used included Tuj-1, GFAP, MBP,

iNOS, Arg-1, CD68 and NF (all from Abcam, Cambridge, UK). The secondary antibodies were CY3-labeled goat anti-mouse IgG and Alexa Fluor 488-labeled goat anti-rabbit IgG (both from Servicebio, China).

2.10. WB assay

Cells or tissues were lysed using RIPA buffer (Servicebio, China) supplemented with protease and phosphatase inhibitors. The protein concentration was then assessed with the BCA protein assay kit (Servicebio, China). The protein samples were denatured by adding a protein supersampling buffer and subsequently transferred to a PVDF membrane (Servicebio, China). The membrane was blocked with 5 % skimmed milk for 1 h, followed by incubation with the primary antibody at 4 °C overnight. After washing away any residual antibody with Tris Buffered Saline containing Tween® 20 (TBST), a secondary antibody was added for 30 min. The membranes were then treated with a mixed ECL luminescent solution to visualize the immunoblot, and the results were analyzed using ImageJ software.

2.11. In vivo bioluminescence imaging

Exosome retention in rats was evaluated by in vivo bioluminescence imaging. Following anesthesia with isoflurane, rats were subjected to imaging of PKH26-stained exosomes using the Small Animal In Vivo Imaging System (IVIS Lumina III, USA).

2.12. Establishment of rat spinal cord hemisection model

Female Sprague Dawley (SD) rats (SPF grade, 8 weeks old) were obtained from Beijing Viton Lihua Laboratory Animal Technology Co., Ltd. (Beijing, China) for this study. The rats were randomly assigned to six groups: sham, SCI, GM, GME, GMNP + magnetic stimulation (MS) and GMNPE + MS. Anesthesia was induced using 2 % isoflurane in a mixture of 30 % oxygen and 70 % nitrogen. The dorsal region was prepared by shaving and disinfecting the area. The vertebral plate over the T10 segment was exposed and removed to access the spinal cord. A 4 mm right hemisection of the spinal cord was performed at the T9-10 level. Hydrogel was then applied to the spinal cord defect, and the muscle and skin were sutured separately. Postoperatively, all rats received daily subcutaneous injections of penicillin (20 mg/kg), and their bladders were manually emptied twice daily for one week. Rats in the GMNPE + MS group were treated with a pulsed magnetic field (15 mT, 60 Hz, 50 % duty cycle) generated by a Helmholtz coil for 30 min each day.

2.13. Basso–Beattie–Bresnahan (BBB) locomotor rating

Two blinded observers assessed the hindlimb movements of rats using the 21-point Basso-Beattie-Bresnahan (BBB) locomotion test. The rats were allowed to move freely in an open field for 15 min each session, and this procedure continued for 8 weeks.

2.14. Open field test

Autonomic motor function in rats was evaluated using the Cleversys TopScanLite device (Cleversys, Virginia, USA). Each rat was acclimated to the assessment environment for 30 min prior to testing. During the evaluation, the rats were placed in a 40 × 40 cm open field, where a high-speed video camera recorded their movements for 10 min. Key parameters, including the number of times the rats crossed the central area, total distance traveled, and average speed, were measured to assess their autonomic function and emotional state. To eliminate any potential influence of previous odors on the results, the field was thoroughly cleaned and disinfected with alcohol between each assessment.

2.15. Electrophysiologic detection of motor neuron excitability

The H-reflex in rats was measured using an eight-channel electrophysiological recorder, PowerLab (ADInstruments, New South Wales, Australia). The animals were immobilized on an operating table and anesthetized with 2 % isoflurane. A needle electrode was inserted into the medial aspect of the ankle joint to stimulate the tibial nerve and induce plantarflexion. The resulting signals were amplified and filtered to obtain an electrogram.Twenty successive electrical stimuli were delivered at frequencies of 0.1, 0.5, 1, 2, and 5 Hz. Data analysis was conducted using LabChart software (version 8.0, ADInstruments, Dunedin, NSW, Australia), focusing on the last 15 of the 20 stimuli for H-wave analysis. Frequency-dependent suppression (RDD) of the H-reflexes was calculated by dividing the mean peak H-wave values at 0.5, 1, 2, and 5 Hz by the mean peak H-wave value at 0.1 Hz.

2.16. Statistical analysis

Statistical analyses were conducted using SPSS version 20.0 (IBM, Armonk, NY, USA). Comparisons between two groups were made using the independent samples *t*-test, while multiple groups were analyzed with one-way ANOVA followed by Bonferroni post hoc tests. Data are presented as mean ± standard deviation, and p values less than 0.05 were regarded as significant. Graphing was performed using GraphPad Prism version 9.0 (LLC, San Diego, CA, USA) and ImageJ (USA).

3. Results

3.1. Synthesis and characterization of Fe_3O_4@$BaTiO_3$

Fe_3O_4 nanoparticles were synthesized using a solvothermal reaction, combining $FeCl_3$ with sodium acetate in an ethylene glycol solution. An aqueous mixture of barium hydroxide and potassium hydroxide was then prepared and stirred. Tetrabutyl titanate was added to this mixture, followed by the Fe_3O_4 nanoparticles. This process led to the hydrolysis and condensation of tetrabutyl titanate, resulting in a vigorous hydrothermal reaction that facilitated the deposition of $BaTiO_3$ nanoparticles onto the Fe_3O_4 nanoparticles, ultimately forming a core-shell structure of Fe_3O_4@$BaTiO_3$.

The morphology of the Fe_3O_4@$BaTiO_3$ nanoparticles was examined by SEM (Fig. 1A). The results indicated that the initially smaller Fe_3O_4 nanoparticles formed shells through the in situ deposition of $BaTiO_3$ following the solvothermal reaction. TEM images further validated the presence of the core-shell structure, revealing a shell layer approximately 10–20 nm thick surrounding the Fe_3O_4 core. High-resolution TEM images showed a spacing of 0.4 nm within the shell layer, consistent with the lattice spacing of the tetragonal 0001 surface (Fig. 1B). Energy dispersive X-ray spectroscopy (EDX) results confirmed the presence of Fe_3O_4 at the core of the nanoparticles, with barium (Ba) and titanium (Ti) detected on the surface (Fig. 1C). This finding further validated the successful synthesis of $BaTiO_3$ on the Fe_3O_4 nanoparticles. DLS analysis revealed an average hydrated particle size of 179.78 nm for Fe_3O_4, while the Fe_3O_4@$BaTiO_3$ nanoparticles exhibited a larger average size of 250.46 nm, supporting the formation of the core-shell structure (Fig. S1). The crystal structures of both Fe_3O_4 and Fe_3O_4@-$BaTiO_3$ nanoparticles were investigated by X-ray diffraction (XRD) (Fig. 1D). The diffraction peaks of Fe_3O_4 were consistent with a cubic spinel structure, whereas the peaks for Fe_3O_4@$BaTiO_3$ corresponded to a chalcogenide structure. Collectively, these results demonstrated the successful coating of $BaTiO_3$ on Fe_3O_4.

Subsequently we investigated the magneto-electric properties of Fe_3O_4@$BaTiO_3$ nanoparticles. The saturation magnetization of both Fe_3O_4 and Fe_3O_4@$BaTiO_3$ was measured at 300 K by VSM. The hysteresis curves showed no intersections with the X-axis or Y-axis, indicating the absence of coercivity and remanent magnetization, which confirmed the strong superparamagnetic properties of the materials

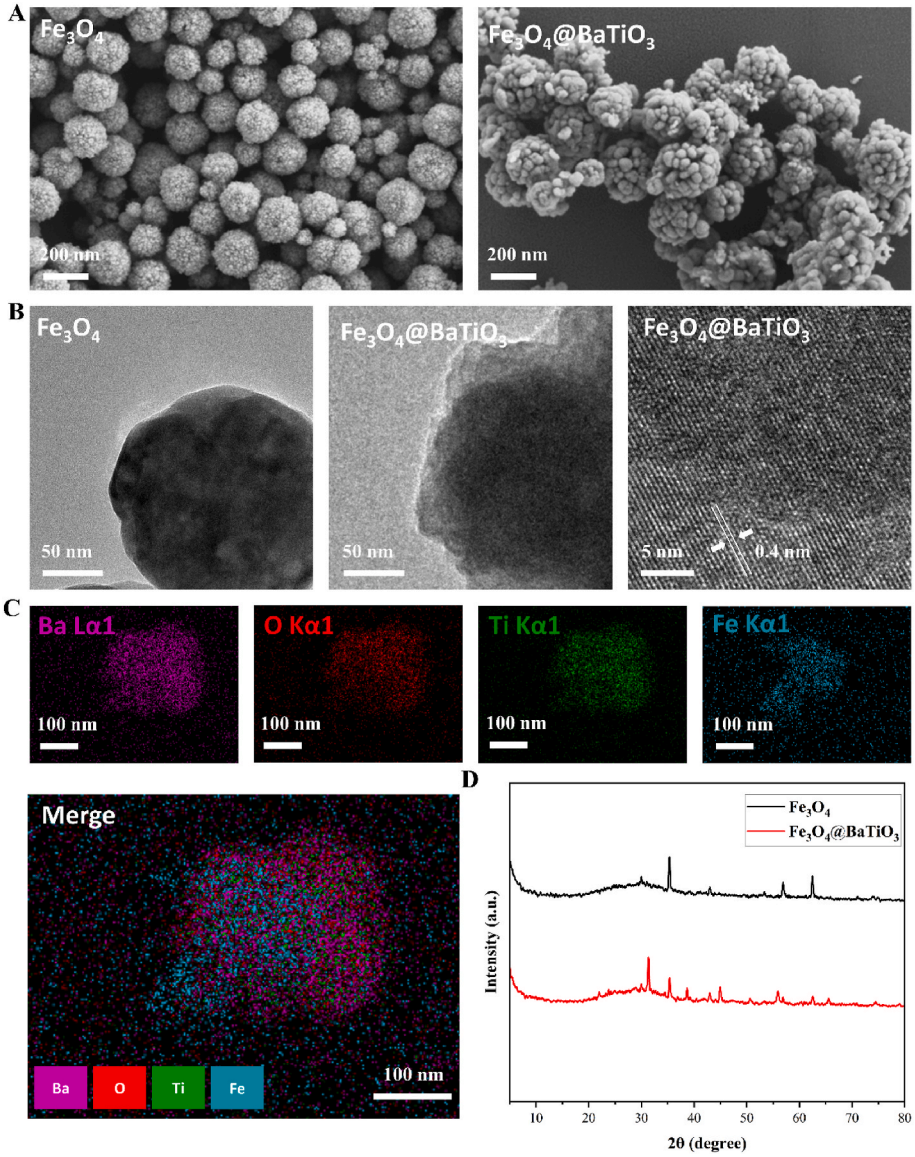

Fig. 1. Characterization of Fe_3O_4@$BaTiO_3$ nanoparticles. (A) SEM images of Fe_3O_4 and Fe_3O_4@$BaTiO_3$ nanoparticles. (B) TEM images of Fe_3O_4 and Fe_3O_4@$BaTiO_3$ nanoparticles, and high-resolution TEM image of Fe_3O_4@$BaTiO_3$ nanoparticles. (C) EDX mapping of Fe_3O_4@$BaTiO_3$ nanoparticles. (D) XRD result of Fe_3O_4 and Fe_3O_4@$BaTiO_3$ nanoparticles.

(Fig. S2). Since $BaTiO_3$ is inherently non-magnetic, its strong binding to the surface of Fe_3O_4 increases the mass and size of the composite while also restricting the movement of magnetic dipoles. As a result, the saturation magnetization of Fe_3O_4@$BaTiO_3$ was reduced to 24.1 emu g^{-1}, compared to 87.4 emu g^{-1} for Fe_3O_4. The piezoelectric properties of the Fe_3O_4@$BaTiO_3$ nanoparticles were evaluated by AFM. The morphology, phase, and amplitude characteristics were presented in Fig. S3. The brightness in the AFM images reflected localized displacement caused by the electric field applied at the scanning probe tip, confirming that the piezoelectric response of the material was measurable. Additionally, the morphology images indicated that the nanoparticles had an average size of approximately 200 nm, consistent with the amplitude and phase images. The piezoresponse amplitude curves exhibited horizontal displacements with characteristic butterfly curves upon voltage changes at specific test points on the material surface (Fig. S4). Additionally, the piezoresponse phase loop images revealed a phase switch of nearly 180°, illustrating the polarization reversibility between two antiparallel states when an external electric field was applied (Fig. S5). These findings confirmed that Fe_3O_4@$BaTiO_3$ nanoparticles possessed strong magneto-electric and piezoelectric properties.

3.2. Extraction and characterization of HUMSC-Exos

Firstly, the isolated HUMSC-Exos were subjected to nanofluidic detection. As shown in Fig. 2A, the average particle size was 81.1 nm (gating range 47.1–190.0 nm). TEM images (Fig. 2B) revealed the characteristic cup shape of the exosomes. Furthermore, the presence of positive markers CD9, CD81, and Alix on the exosome surface, along with the absence of the negative marker Calnexin (Fig. 2C), confirmed the successful extraction of HUMSC-Exos. Given the potential impact of UV irradiation during hydrogel synthesis on the integrity and functionality of exosomes, we systematically re-characterized HUMSC-Exos exposed to 15-s UV irradiation. As shown in Fig. S6, no significant alterations were observed in the particle size distribution of UV-treated HUMSC-Exos (average diameter: 124.3 nm, representing 93.8 % of the population). TEM further confirmed the preservation of their characteristic cup-shaped morphology. WB analysis demonstrated successful

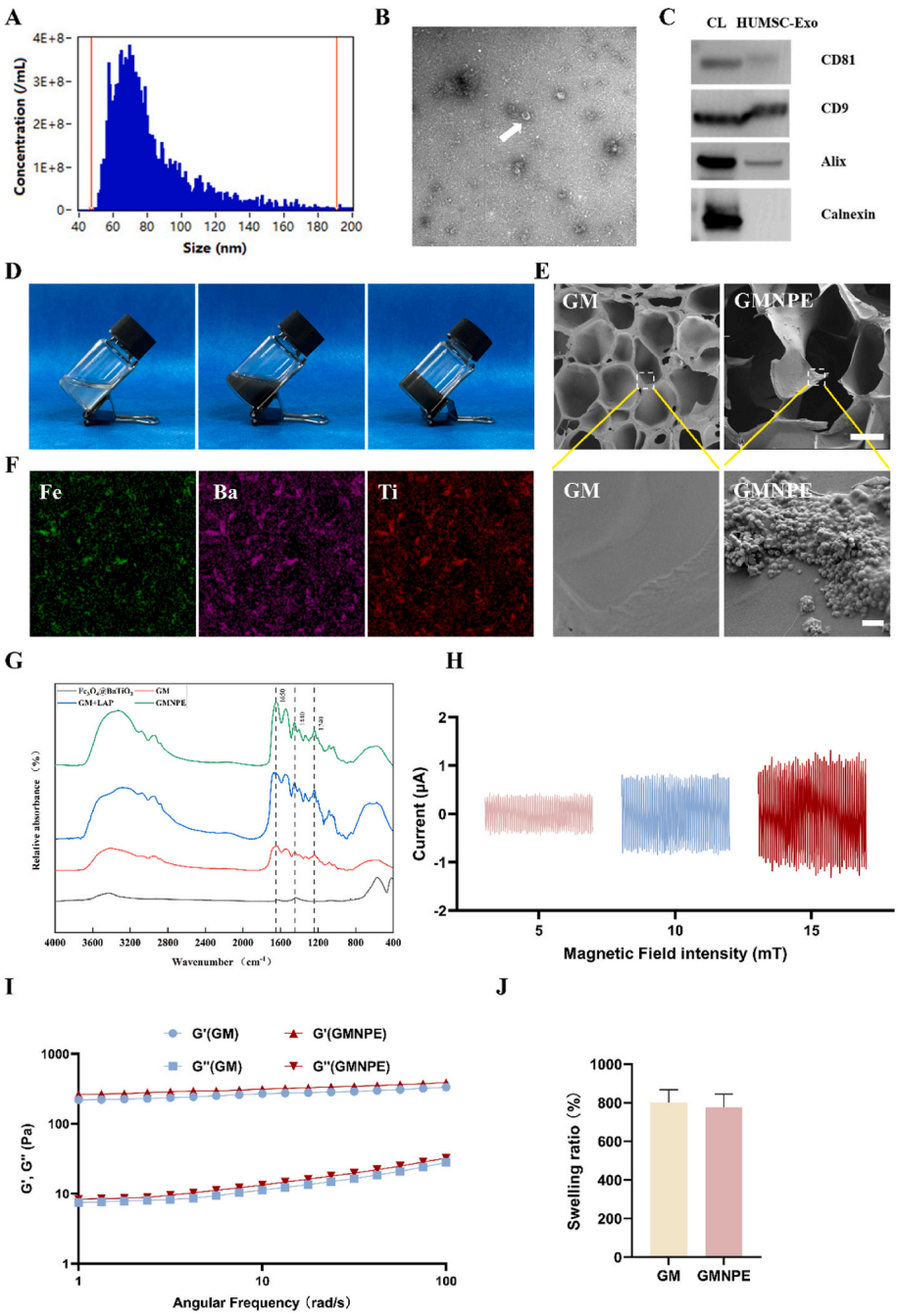

Fig. 2. Characterization of the HUMSC-Exos and GMNPE hydrogels. (A) The analysis results of Flow NanoAnalyzer showing exosomes with a particle size of 81.1 nm (gating range 47.1–190.0 nm). (B) TEM image revealed the characteristic cup shape (white arrow) of the exosomes. (C) WB results showing that exosomes positively expressed CD9, CD81, and Alix, along with the absence of the negative marker Calnexin. (D) different states of hydrogels: GM hydrogel before gel formation (left), GMNPE hydrogel before gel formation (middle), GMNPE hydrogel after gel formation (right). (E) SEM images of GM hydrogel and GMNPE hydrogel at low and high magnification. Scale bar: 100 μm. Scale bar of magnified image: 1 μm. (F) EDX mapping of GMNPE hydrogel. (G) FTIR spectra of the Fe_3O_4@$BaTiO_3$, GM hydrogel, GM + LAP hydrogel, and GMNPE hydrogel. (H) The output current of GMNPE hydrogel under magnetic field stimulation (5 mT, 10 mT and 15 mT). (I) The mechanistic properties of GM and GMNPE hydrogels. (J) Swelling properties of GM and GMNPE hydrogels (n = 4).

expression of three exosomal positive markers, while negative markers showed no detectable expression.

3.3. Fabrication and characterization of the GMNPE hydrogels

Reconstructing the microenvironment with multifunctional hydrogels has proven to be an effective strategy for promoting accelerated repair of SCI [47]. In this study, GMNPE hydrogels were prepared through a three-step synthesis process, as illustrated in Scheme 1. First, Fe_3O_4@$BaTiO_3$ was incorporated into the GelMA solution and thoroughly mixed. Next, HUMSC-Exos droplets were added to the hydrogel and allowed to incubate overnight. Finally, a photoinitiator was uniformly added to obtain the GMNPE hydrogel. Fig. 2D illustrated the hydrogel's appearance before and after formation. SEM results depicted the microscopic morphology of GM and GMNPE in Fig. 2E. Both hydrogels exhibited an irregular, loose, and porous structure, which promoted neuronal cell attachment and supports the growth of nerve fibers [48]. The EXD mapping of the GMNPE hydrogel also illustrated

that Fe_3O_4@$BaTiO_3$ nanoparticles were uniformly distributed throughout the hydrogel (Fig. 2F). FTIR results showed (Fig. 2G) that all groups of hydrogels exhibited distinct FTIR characteristic peaks: 2930 cm^{-1} (CH), 1650 cm^{-1} (C═O of amide I), 1310-1470 cm^{-1} (CH), 1440 cm^{-1} (C-N), and 1240 cm^{-1} (N-H of amide III). These findings suggested that the incorporation of MENPs did not alter the bonding characteristics of the hydrogels. To detect the output current generated by GMNPE under the influence of a magnetic field, a low-power current analyzer was employed. As illustrated in Fig. 2H, the output current by GMNPE (1%wt Fe_3O_4@$BaTiO_3$) increased with the augmentation of magnetic field intensity. Under a magnetic field strength of 15 mT, the output current reached a maximum of 1.2 μA. In conjunction with previous studies, it has been demonstrated that microampere-level currents can effectively promote the differentiation of NSCs into neurons [47,49]. As depicted in Fig. S7, the hydrogel exhibited continuous and stable degradation over a period of 6 weeks, achieving a degradation rate of 83.42 %. Concurrent with the gradual degradation of GMNPE, the intensity of the output current also decreased. However, the system was capable of providing stable electrical stimulation for at least 4 weeks, as illustrated in Fig. S8. The rheological results demonstrated that the storage moduli (elastic modulus, G′) of the hydrogels exceeded the loss moduli (viscous modulus, G″) across the angular frequency range of 1–100 Hz, indicating excellent stability (Fig. 2I). Additionally, the mechanical properties of these hydrogels aligned well with the mechanics of neural tissue (0.1–3 kPa), which supported the growth and differentiation of neural cells [50,51]. The swelling ratio of GM and GMNPE hydrogels were approximately 802 ± 65 % and 777 ± 69 %, respectively. The introduction of Fe_3O_4@$BaTiO_3$ slightly reduced the swelling ratio of GMNPE hydrogels compared to GM hydrogels, though the difference was not statistically significant (Fig. 2J). Furthermore, the swelling ratio and mechanical properties of the GMNPE hydrogels remained stable after immersion in physiological media for 7 and 14 days (Fig. S9). This stability indicated that the hydrogels maintained both long-term swelling capabilities and mechanical integrity.

In addition, in vivo imaging results indicated that GMNPE hydrogels loaded with exosomes stained with PKH26 retained a significant amounts of exosomes five days after implantation at the injury site in rats. In contrast, rats in the exosome-loaded PBS-only group showed negligible levels of detectable exosomes after the same period (Fig. S10). These findings confirmed that the hydrogel effectively prolonged the retention and release of exosomes at the injury site.

3.4. Biocompatibility and biodegradability of hydrogels

To assess the biocompatibility and potential toxicity of GMNPE, NSCs were cultured on hydrogels containing varying concentrations of Fe_3O_4@$BaTiO_3$ and subjected to daily peripheral magnetic field stimulation. The survival of NSCs was evaluated on days 1, 4, and 7 using live-dead staining (Fig. S11). The hydrogels were categorized into control groups and GMNPE groups with concentrations of 0.5 %, 1 %, and 2 % (wt). The 0.5 % (GMNPE0.5) and 1 % (GMNPE1) groups showed no significant differences in NSC survival compared to the control. However, at a concentration of 2 % (GMNPE2), there was a marked reduction in cell survival, indicating that a higher concentration of Fe_3O_4@$BaTiO_3$ may exhibit cytotoxic effects (Fig. S12). Moreover, results from the CCK-8 assays corroborated the live-dead staining findings, revealing that the 1 % concentration of Fe_3O_4@$BaTiO_3$ promoted the highest cell proliferation viability (Fig. S13). Consequently, group GMNPE1 was selected for subsequent experiments.

Hydrogels undergo gradual degradation following implantation in the body. Therefore, suitable bioscaffolds must ensure that neither the hydrogels nor their degradation products induce toxicity in the body's organs and tissues [52,53]. In the present study, GMNPE hydrogels were implanted in SCI rats and divided into GMNPE and GMNPE + MS groups, and were evaluated for biosafety along with sham group as well as SCI group rats. The results indicated no significant pathological changes in the major organs—heart, liver, spleen, lungs, and kidneys—across all groups (Fig. S14). Furthermore, liver function markers (ALT and AST) were within the normal range, showing no significant differences among the groups (Figs. S15–16). These findings demonstrated that the implantation of GMNPE hydrogel was not significantly toxic to rats regardless of the presence or absence of magnetic field stimulation and could be used as a safe treatment.

3.5. Anti-inflammatory effects of GMNPE in vitro

Microglia can be subdivided into pro-inflammatory M1 type and anti-inflammatory M2 type, in which the markers of M1 type microglia include protein-inducible nitric oxide synthase (iNOS), tumor necrosis factor-alpha (TNF-α), and interleukin (IL-6), and the markers of M2 type microglia include arginase-1 (Arg-1) and IL-10 [54]. To verify the anti-inflammatory effect of GMNPE hydrogel, GMNPE hydrogel was co-cultured with mouse microglia BV2 cell line. Initially, the microglia were activated by LPS, and the activated microglia showed enlarged cytosol, increased number of shorter protrusions and became more complex in morphology [55]. Subsequently, a large number of exosomes labeled with the red dye PKH26 could be observed in the cytoplasm of BV2 cells (Fig. 3A), which implied that exosomes released by GMNPE were successfully endocytosed by BV2 cells. The optimal anti-inflammatory concentration of exosomes was determined through a concentration gradient experiment, and GMNPE hydrogels were prepared with a HUMSC-Exos concentration of 4 μg/μl (Fig. S17).

The results of immunofluorescence staining demonstrated a significant increase in the number of cells positive for iNOS, a marker of pro-inflammatory M1-type microglia, following LPS stimulation compared to the CON group. Conversely, the number of cells positive for Arg-1, a marker of anti-inflammatory M2-type microglia, was significantly reduced. In the GME group, the expression of iNOS was markedly decreased compared to the LPS group, while Arg-1 expression was significantly increased, indicating that HUMSC-Exos exerted an inhibitory effect on inflammation. Furthermore, the GMNP + MS group exhibited a moderate reduction in iNOS expression and a modest increase in Arg-1 expression relative to the LPS group, suggesting that the electrical stimulation generated by GMNP + MS also contributed to a partial alleviation of inflammation, albeit to a lesser extent than that observed in the GME group. Finally, the results from the GMNPE + MS group revealed that the hydrogel, under the combined influence of HUMSC-Exos and electrical stimulation, exerted a more pronounced anti-inflammatory effect. This anti-inflammatory efficacy was superior to that achieved by either the exosome-alone group (GME) or the electrical stimulation-alone group (GMNP + MS) (Fig. 3B–E). WB analysis revealed that the protein expression of iNOS was significantly reduced in both the GME and GMNP + MS groups compared to the LPS group, while the expression of Arg-1 was markedly increased. The GMNPE + MS group exhibited even lower iNOS protein expression and higher Arg-1 expression than both the GME and GMNP + MS groups, demonstrating that GMNPE + MS possesses the most potent anti-inflammatory capability (Fig. 3F–H). Consistent with these findings, qPCR results showed a similar trend. Statistical analysis indicated that the mRNA expression levels of pro-inflammatory cytokines (iNOS, TNF-α, and IL-6) in LPS-activated BV2 cells were significantly elevated compared to the control group, while the mRNA expression of anti-inflammatory cytokines (Arg-1 and IL-10) was significantly reduced. In the GME and GMNP + MS groups, the expression of pro-inflammatory cytokines was decreased, and the expression of anti-inflammatory cytokines was increased. Notably, the GMNPE + MS group exhibited the lowest expression of pro-inflammatory cytokines and the highest expression of anti-inflammatory cytokines (Fig. 3I–J). Additionally, we compared the anti-inflammatory effects of GMNP and GMNPE hydrogels in the absence of a magnetic field, as well as the impact of the magnetic field itself on BV2 cells and exosomes. The results demonstrated that the presence of an external magnetic field did not significantly affect BV2

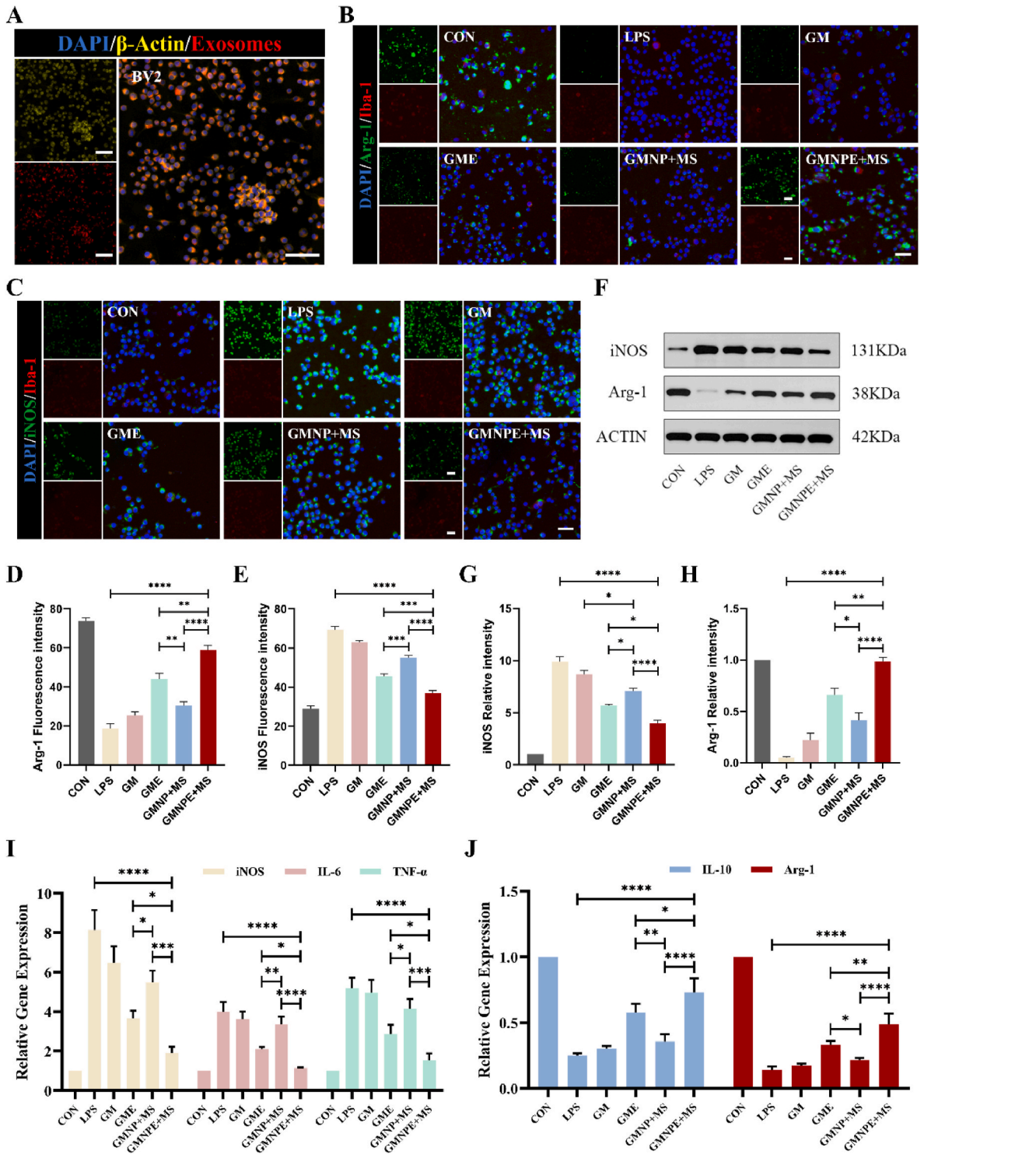

Fig. 3. Anti-inflammatory effects of GMNPE in vitro. (A) BV2 cells cultured on GMNPE hydrogels can normally phagocytose PKH26-stained HUMSC-Exos released from hydrogels. Scale bars: 100 μm. (B–C) Immunofluorescence images of BV2 cells cultured in each group. Cells were stained red with ionized calcium-binding adaptor molecule 1, and Arg-1/iNOS was stained green. Scale bar: 50 μm. (D–E) Quantification of fluorescence intensity of Arg-1 and iNOS level in each group (n = 5). (F) Western blot images showed the changes in protein expression of iNOS and Arg-1. (G–H) Quantitative analysis of iNOS/Actin and Arg-1/Actin ratio (n = 3). (I) RT-qPCR results of the pro-inflammatory cytokines iNOS, IL-6 and TNF-α (n = 3). (J) RT-qPCR results of the anti-inflammatory cytokines Arg-1 and IL-10 (n = 3). Significance: ns-not significant, *p < 0.05, **p < 0.01, ***p < 0.001, ****p < 0.0001.

cells or HUMSC-Exos. Furthermore, GMNP alone, without the magnetic field, did not exhibit significant anti-inflammatory effects. Only the combination of Fe_3O_4@$BaTiO_3$ and the magnetic field produced a more pronounced anti-inflammatory effect (Figs. S18–19).

In summary, these findings collectively demonstrate that HUMSC-Exos significantly inhibit inflammation, and electrical stimulation also exhibits a certain degree of anti-inflammatory capability. The GMNPE + MS group, under the combined influence of HUMSC-Exos and electrical stimulation, exerted a more robust anti-inflammatory effect. In the early stage of SCI, a substantial number of activated microglia in the affected

area produce pro-inflammatory factors, leading to damage to the surviving nerve cells. Within 24–48 h, these microglia recruit and activate macrophages, resulting in additional harm to neuronal cells at the injury site [56]. Therefore, GMNPE can play a crucial role in suppressing inflammation in the early stages of SCI by promoting microglial M2 polarization.

3.6. NSCs differentiation and axon regeneration on GMNPE hydrogels in vitro

NSCs have multiple differentiation potentials and are self-renewing cells that can differentiate into three cell sublineages, neurons, astrocytes, and oligodendrocytes [57]. In neural tissue engineering, how to induce differentiation of NSCs to neurons rather than astrocytes is key to restoring neural connectivity as well as inhibiting glial scar formation. Partial study indicates that electrical stimulation influences the fate of NSCs [13,14]. Despite the potential of MENPs, the effects of their electrical stimulation on NSCs differentiation remain underexplored. To address this gap, we investigated how electrical stimulation from these nanoparticles, influenced by a peripheral magnetic field, affects NSCs. NSCs were placed in a Helmholtz coil capable of generating a stable magnetic field to receive stimulation and the NSC differentiation was observed. In light of the established regulatory effects of inflammatory microenvironment on neural regeneration during SCI recovery [58], neuroinflammatory conditions were replicated in vitro by supplementing NSC cultures across experimental groups with supernatant derived from LPS-activated BV2 microglial cultures, thereby recapitulating pathophysiological neuroinflammatory cascades post-SCI. NSC morphological and functional assessments were systematically conducted following 7-day culture under these simulated inflammatory conditions. The immunofluorescence staining results indicated that the proportion of newly generated neuronal marker β-III tubulin (Tuj-1) (+) cells in the GMNPE + MS group was approximately 14.1 %, significantly higher than that in the GMNP + MS group (8.6 %), the GME group (5.4 %), and the LPS group (1.7 %). Moreover, the proportion of oligodendrocyte marker myelin basic protein (MBP) (+) cells in the GMNPE + MS group was also significantly higher than that in the GMNP + MS group, the GME group, and the LPS group (16.6 % vs. 10.6 %, 5.3 %, and 0.54 %, respectively). In contrast, the proportion of astrocyte marker GFAP (+) cells in the GMNPE + MS group was only 15.4 %, significantly lower than in the other groups (Fig. 4B–E). These results suggest that NSCs in the GMNPE + MS group preferentially differentiated into neurons and oligodendrocytes rather than astrocytes. Subsequently, the axonal regeneration in each group was assessed by evaluating the expression of the axon-associated protein neurofilament (NF). The immunofluorescence staining results revealed that the average axonal length in the GMNPE + MS group reached 202.8 μm, significantly greater than that in the GMNP + MS group (149.5 μm), the GME group (95.0 μm), and the LPS group (16.7 μm). The proportion of NF-positive area in the GMNPE + MS group (21.4 %) was also significantly higher than that in the other groups (Fig. 4B–F-G). These findings indicate that axonal growth and neural network formation in the GMNPE + MS group outperformed those in the other groups. WB results exhibited a similar trend, with significantly higher protein expression levels of Tuj-1, MBP, and NF in the GMNPE + MS group, while GFAP protein expression was markedly lower (Fig. 4H–L). The results of qPCR statistical analysis were consistent with the aforementioned findings, exhibiting the same trend (Fig. 4M). To ensure experimental rigor, we systematically validated the biological effects of GMNP on NSCs under non-magnetic conditions. The results demonstrated no significant difference in NSCs differentiation between the GMNP group and the LPS group. Crucially, MENPs under non-magnetic conditions failed to effectively regulate NSCs differentiation or promote axonal regeneration, as evidenced by quantitative morphological analysis (Fig. S20). This critical control experiment confirms the magnetic field-dependency of the observed therapeutic effects, reinforcing the specificity of our intervention strategy.

It is noteworthy that we observed a significantly higher proportion of Tuj-1 (+) cells and MBP (+) cells in the GME group compared to the LPS group, alongside a significantly lower proportion of GFAP (+) cells and a markedly elevated expression of NF. The results from WB and qPCR corroborated these findings. These results suggest that HUMSC-Exos possess a certain capability to promote the differentiation of NSCs and axonal regeneration, which is consistent with previously reported studies on mesenchymal stem cell exosomes [59,60]. However, in this study, the capacity of HUMSC-Exos to promote differentiation and axonal regeneration was limited, being less effective than the stimulation effects induced by electrical stimulation (GMNP + MS). Nevertheless, the GMNPE + MS group demonstrated the most pronounced effects, outperforming both the GMNP + MS and GME groups. This indicates that under the combined influence of the electrical stimulation generated by MENPs and HUMSC-Exos, GMNPE can induce NSCs to differentiate into newly formed neurons and oligodendrocytes that are beneficial for neural function regeneration, while suppressing differentiation into astrocytes, and simultaneously promoting axonal regeneration and neural network formation (Fig. 4A).

3.7. Mechanisms underlying GMNPE + MS-induced directed differentiation of NSCs and axonal growth promotion

To further investigate the mechanisms underlying GMNPE + MS-induced directed differentiation of NSCs and axonal growth, we performed RNA sequencing on NSCs treated with GMNPE + MS for 7 days. Comparative analysis between the GMNPE + MS and control groups revealed 1916 differentially expressed genes, including 1211 upregulated and 705 downregulated genes (Fig. 5A). GO enrichment analysis of these differentially expressed genes demonstrated significant associations with molecular processes critical for neurogenesis and differentiation, such as protein binding, axon guidance, axon development, nervous system development, and neuronal cell body morphogenesis (Fig. 5B). KEGG pathway analysis further identified multiple signaling cascades enriched in the GMNPE + MS group, including neuroactive ligand-receptor interactions, calcium signaling, PI3K-Akt signaling, MAPK signaling, and cAMP signaling pathways (Fig. 5C). These pathways are closely associated with the differentiation of NSCs and neural regeneration. For instance, the calcium signaling pathway can negatively regulate the PTEN protein, which serves as a major intrinsic barrier to axonal regeneration [61,62]. The MAPK signaling pathway plays a crucial role in neuronal differentiation, growth, survival, and axonal regeneration following central nervous system injury [63]. Additionally, cAMP signaling is essential for neurite growth and axonal guidance; stimulating intracellular cAMP activity can significantly enhance neuronal survival and axonal regeneration after SCI [64].

Notably, the PI3K-Akt pathway—a well-documented regulator of NSC fate determination—was highlighted by the enrichment of 50 differentially expressed genes. Prior studies have established that PI3K-Akt activation promotes NSC differentiation toward neuronal lineages while suppressing astrocytic commitment, and critically enhances post-injury axonal regeneration [47,65–67]. To validate this, WB analysis confirmed significantly elevated phosphorylation levels of PI3K (p-PI3K) and Akt (p-Akt) in the GMNPE + MS group compared to controls (Fig. 5D, S21). These findings further suggest that the PI3K-Akt pathway may be involved in mediating the directed differentiation and axonal regeneration of NSCs induced by GMNPE + MS.

3.8. GMNPE hydrogel promoted functional recovery in SCI rats

In order to verify the effectiveness of GMNPE hydrogel in the treatment of SCI in vivo under the effect of magnetic stimulation, we established a semi-transverse SCI model in SD rats and evaluated the recovery of motor function. As illustrated in Fig. S22, the T10 segmental spinal cord of rats was exposed, and an incision of about 4 mm length was made in the right spinal cord. The rats were divided into 4 groups: sham

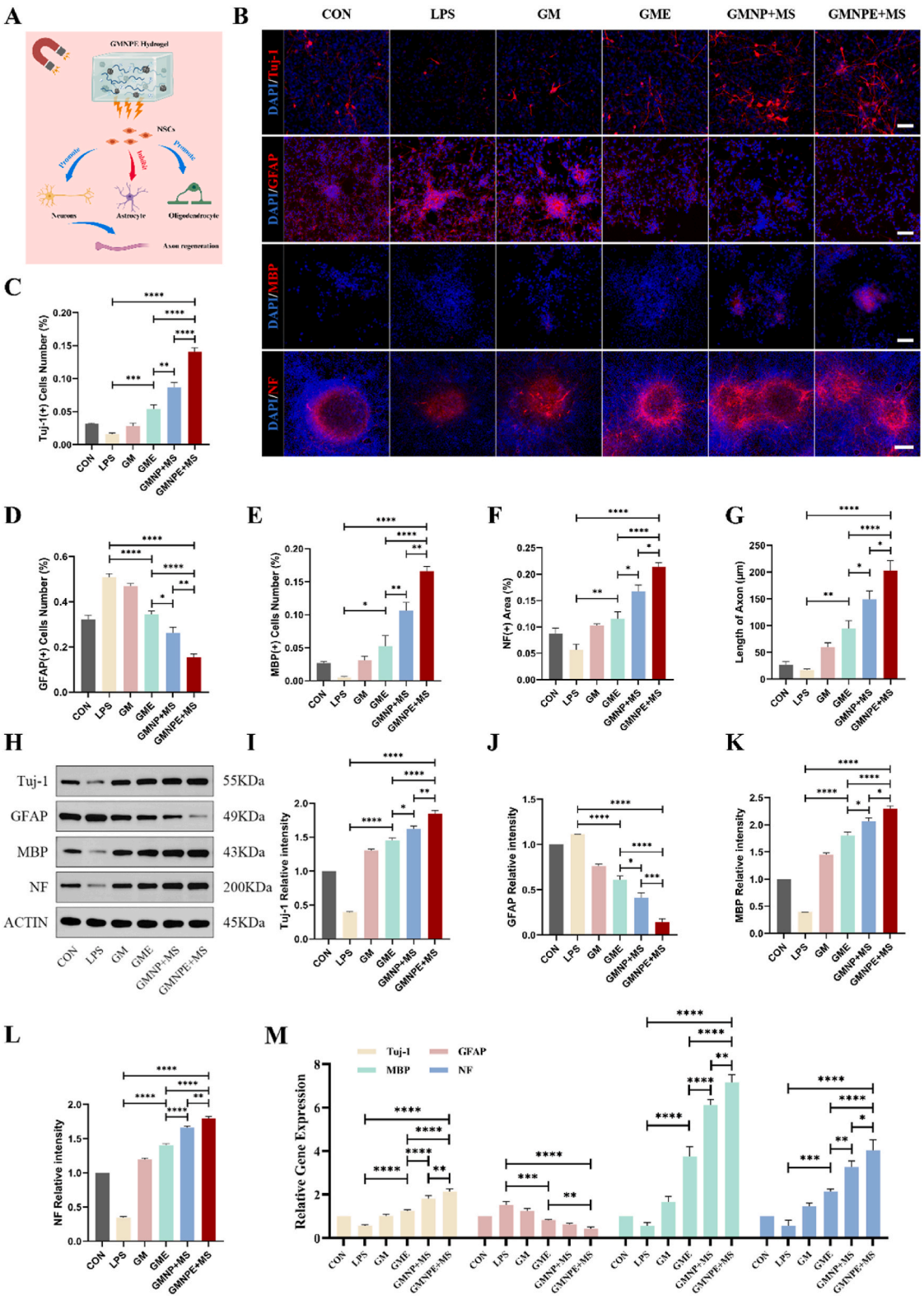

Fig. 4. NSCs differentiation and axon regeneration on hydrogels. (A) An illustration of GMNPE hydrogel promoting NSCs differentiation to neurons and oligodendrocytes and axon regeneration. (B) Immunofluorescence staining of NSCs cultured on different groups. Red IF represents the neuron marker Tuj-1, astrocyte marker GFAP, oligodendrocyte marker MBP, or neurofilament marker NF respectively. Scale bar: Tuj-1, GFAP, MBP, 50 μm. NF, 150 μm. (C–E) Statistical analysis of the percentage of Tuj-1 (+), GFAP (+) and MBP (+) cells to total cell number (n = 5). (F–G) Statistical analysis of the NF (+) area ratio and the length of NF (+) axon (n = 5). (H) Western blot images showed the changes in protein expression of Tuj-1, GFAP, MBP and NF. (I–L) Quantitative analysis of Tuj-1/ACTIN, GFAP/ACTIN, MBP/ACTIN and NF/ACTIN ratio in Western blot images (n = 3). (M) RT-qPCR analysis of the gene expression of Tuj1, GFAP, MBP and NF (n = 3). Significance: *p < 0.05, **p < 0.01, ***p < 0.001, ****p < 0.0001.

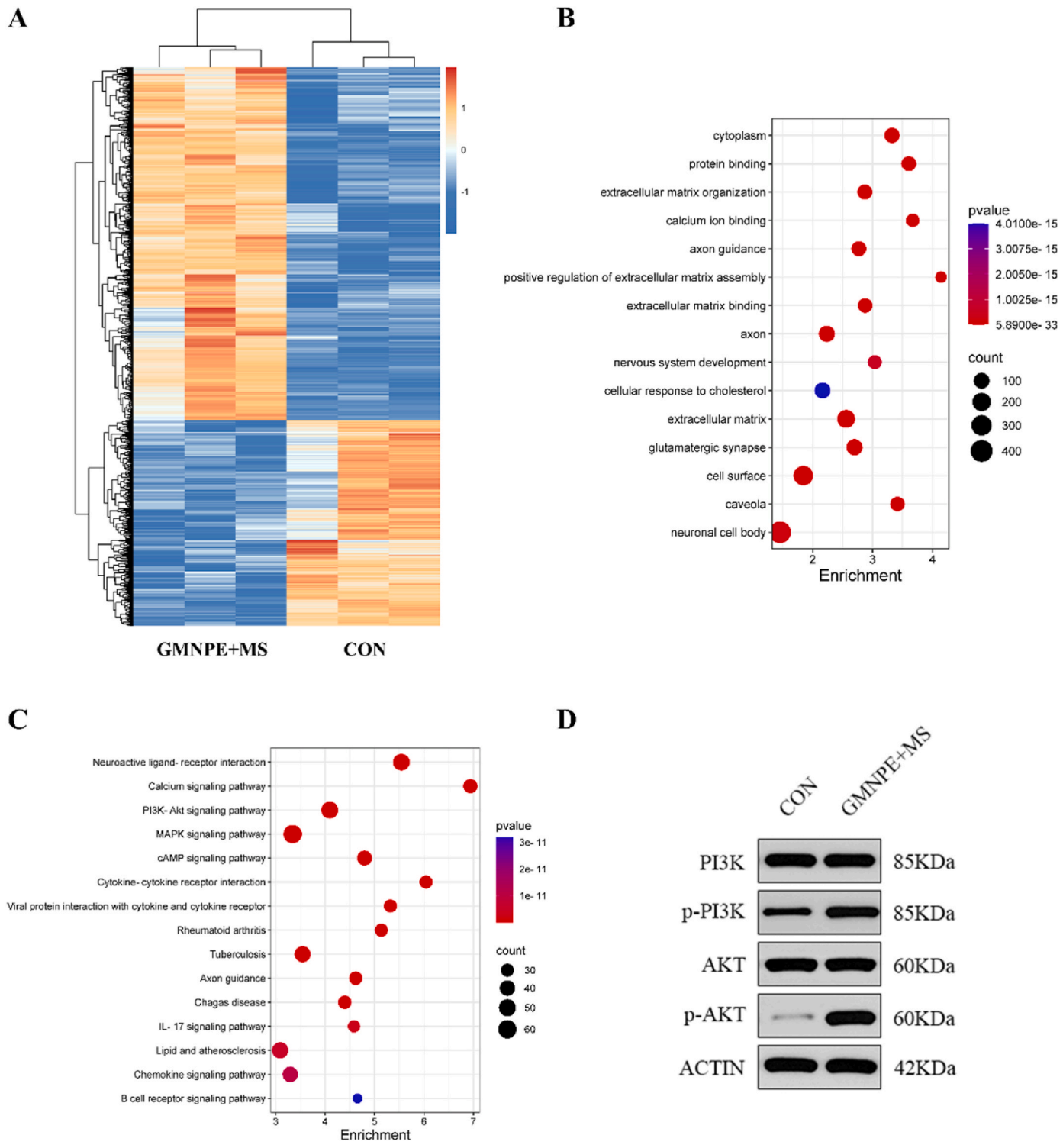

Fig. 5. The mechanism of GMNPE + MS regulating the differentiation of NSCs and axon regeneration. (A) Heatmap illustrating differential genes in the GMNPE + MS group compared to the CON group (log2 Fold change ≥0.5 and q < 0.05). (B) Presentation of the top 15 entries in the bubble diagram of GO enrichment (n = 3). (C) The bubble diagram of KEGG enrichment (n = 3). (D) Western blot images showed the expression of the PI3K-AKT pathway protein between the CON group and the GMNPE + MS group.

group, SCI alone group, GMNPE group, and GMNPE + MS group. Rats in the GMNPE + MS group were treated with a pulsed magnetic field generated by a Helmholtz coil (Fig. S23).

The BBB score was utilized to evaluate the motor function recovery of the rats, and after 8 weeks of SCI, the BBB scores of the right hind limb in both the SCI group and the GM group did not exceed 6, which implied that the body's own self-healing ability was limited. Furthermore, the use of hydrogel treatment alone had minimal impact on the recovery of motor function. In contrast, the motor function recovery of the GMNPE + MS group was statistically more significant than that of the SCI group in 2–4 week postoperatively, indicating that the GMNPE hydrogel under magnetic field stimulation could promote functional recovery in the

subacute phase following SCI. During the 4–8-week post-injury period, the GMNPE + MS group showed rapid motor function recovery, with a BBB score of 12.5 ± 1.6, significantly higher than of the GME group (7.5 ± 0.9) and the GMNP + MS group (9.6 ± 1.2, Fig. 6A). Notably, rats in the GME group demonstrated improved motor function recovery compared to the SCI group. These results indicate that HUMSC-Exos can partially improve motor function recovery in rats, albeit to a lesser extent than the effects generated by electrical stimulation.

Fig. 6B presents a schematic diagram of the open field test conducted on each group of rats 8 weeks postoperatively. The distance traveled, speed, and number of times crossing the center in the open field were compared among the four groups of rats (Fig. 6C–E). The results indicate that rats in the GMNPE + MS group traveled a significantly longer distance in the open field (77.0 ± 18.8m) compared to the SCI group (35.6 ± 12.2m), GME group (48.2 ± 15.8m) and GMNP + MS group (58.3 ± 15.2m). Furthermore, the GMNPE + MS group exhibited a significantly higher speed (10.6 ± 2.1 mm/s) than the SCI group (5.3 ± 1.9 mm/s), GME group (7.6 ± 2.6 mm/s) and GMNP + MS group (8.7 ± 1.4 mm/s). Additionally, the GMNPE + MS group crossed the center area an average of 15.3 ± 4.1 times, which was not significantly different from the sham group (18.5 ± 6.2) but was significantly greater than the SCI group (7.4 ± 3.7), GME group (10.4 ± 3.7) and GMNP + MS group (11.8 ± 3.7). The increased frequency of center zone crossings in GMNPE + MS-treated rats reflected enhanced motor functional recovery, as the central area in the open field test was considered an "anxiogenic zone" due to its open and unshielded nature. Notably, rodents with SCI typically exhibit anxiety-like behaviors (such as pain hypersensitivity and sensorimotor deficits), which further reduce exploratory activity in this aversive region. Conversely, improved motor recovery is physiologically associated with attenuated anxiety phenotypes, leading to elevated center zone

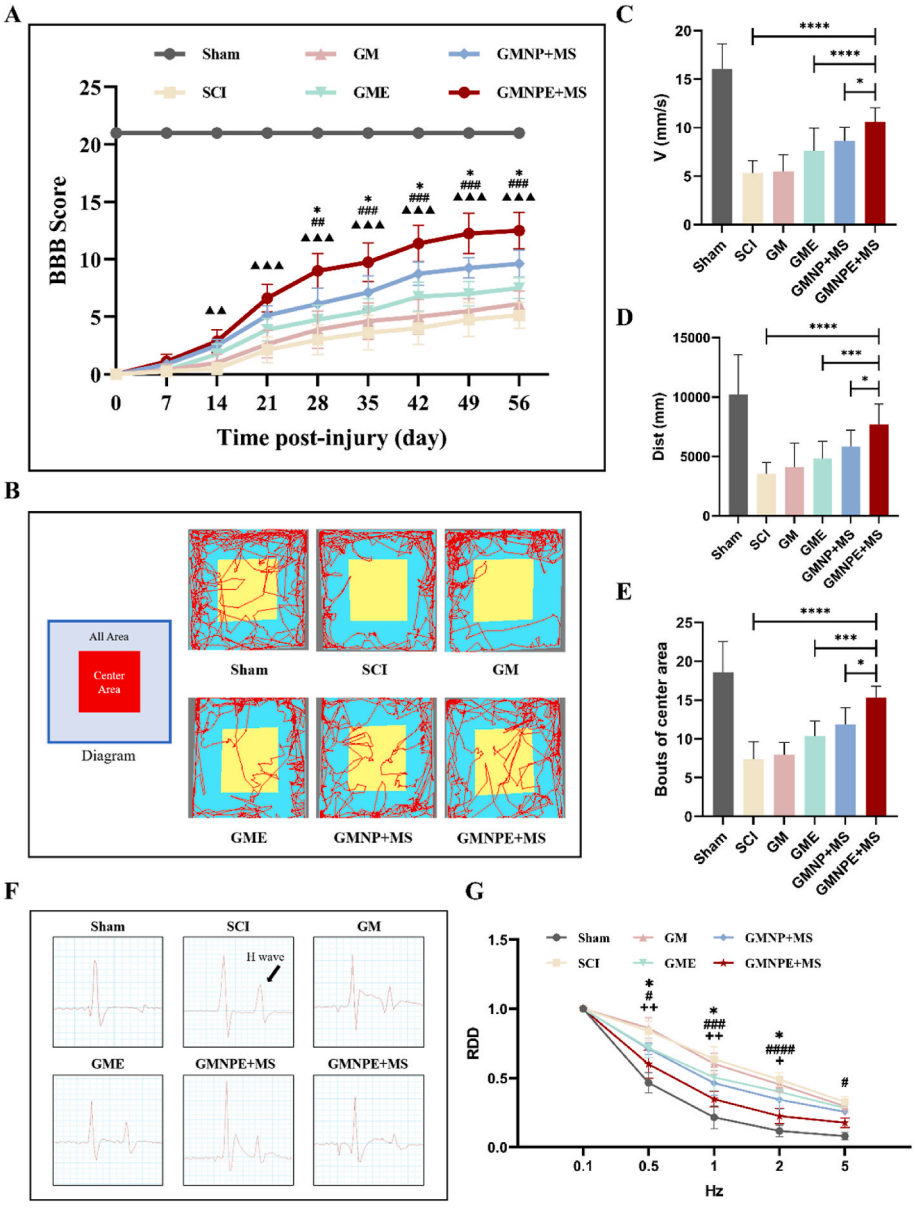

Fig. 6. Functional recovery of rats in different groups. (A) The BBB score of rats in each group (n = 8). (B) An illustration of the open field test. (C–E) Quantitative analysis of distance, speed and bouts of center area for each group in the open field test (n = 8). (F) Electrophysiological detection waveforms of each group. The black arrow represents the H-wave. (G) Results of the analysis of electrophysiological RDD data at 8 weeks after SCI in each group (n = 5). Symbol (*) represented the comparison of the GMNPE + MS group with the GMNP + MS group. Symbol (#) represented the comparison of the GMNPE + MS group with the GME group. Symbol (▲) represented the comparison of the GMNPE + MS group with the SCI group. Symbol (+) represented the comparison of the GMNPE + MS group with the Sham group. Significance: ns-not significant, *p < 0.05, **p < 0.01, ***p < 0.001, ****p < 0.0001.

exploration [68]. A comprehensive assessment of the above data revealed that rats in the GMNPE + MS group exhibit superior motor function recovery compared to other injury groups.

The nerve conduction function of the spinal cord was assessed by electrophysiology, with results presented in Fig. 6F–G. After 8 weeks of SCI, all groups exhibited a similar decline in RDD with increasing stimulation frequency. The RDD of the GMNPE + MS group was significantly lower than that of the GME group as well as the GMNP + MS group at 0.5 Hz, 1 Hz, and 2 Hz frequencies. These findings suggest that the SCI rats experienced motor neuron damage at the injury site, resulting in increased nerve excitability and elevated skeletal muscle tone, which contributed to spasticity. In contrast, the GMNPE + MS treatment diminished upper motor neuron lesions and reduced excitability compared to the GME and GMNP + MS groups, thereby enhancing motor function following SCI.

In addition, bladder dysfunction is a significant concern for patients with SCI, and the functional reserve of the bladder serves as an important indicator of SCI recovery [69]. The bladder wall thickness was assessed by HE staining (Figs. S24–25). The measurements revealed that the bladder wall thickness in the GMNPE + MS group (497.2 ± 61.0 μm) was significantly higher than that in the SCI group (216.9 ± 66.8 μm), GME group (256.8 ± 43.7 μm) and GMNP + MS group (318.8 ± 41.8 μm).

The findings from this series of studies demonstrated that magnetic stimulation combined with GMNPE hydrogel effectively promoted the recovery of motor function, electrophysiological performance, and bladder function in SCI rats.

3.9. GMNPE hydrogel modulated the inflammatory microenvironment in vivo

Following SCI, activated microglia release significant amounts of neurotoxic factors as well as pro-inflammatory factors, resulting in an inflammatory response that usually causes a series of secondary injuries. Therefore, early intervention to suppress inflammation is crucial for the SCI recovery.

The inflammatory response magnitude at the injury site in each treatment group was quantitatively assessed. One week after SCI, the spinal cord of rats in each group were harvested for analysis. Immunofluorescence staining revealed a substantial accumulation of CD68 (+) macrophages in the region surrounding the injury (Fig. 7A). Quantitative analysis demonstrated significantly elevated CD68(+) cell proportions in SCI groups compared to sham controls, indicating robust macrophage activation and consequent inflammatory exacerbation following SCI. Notably, the GME group exhibited marked reduction in CD68(+) cells versus SCI and GM groups, suggesting enhanced anti-inflammatory efficacy through HUMSC-Exos incorporation into hydrogel matrices. Comparative analysis showed GMNP + MS group achieved significant CD68(+) cell reduction relative to SCI group, albeit with attenuated potency compared to HUMSC-Exos-mediated effects, implying synergistic yet subordinate anti-inflammatory contributions from electrical stimulation. Strikingly, GMNPE + MS group displayed

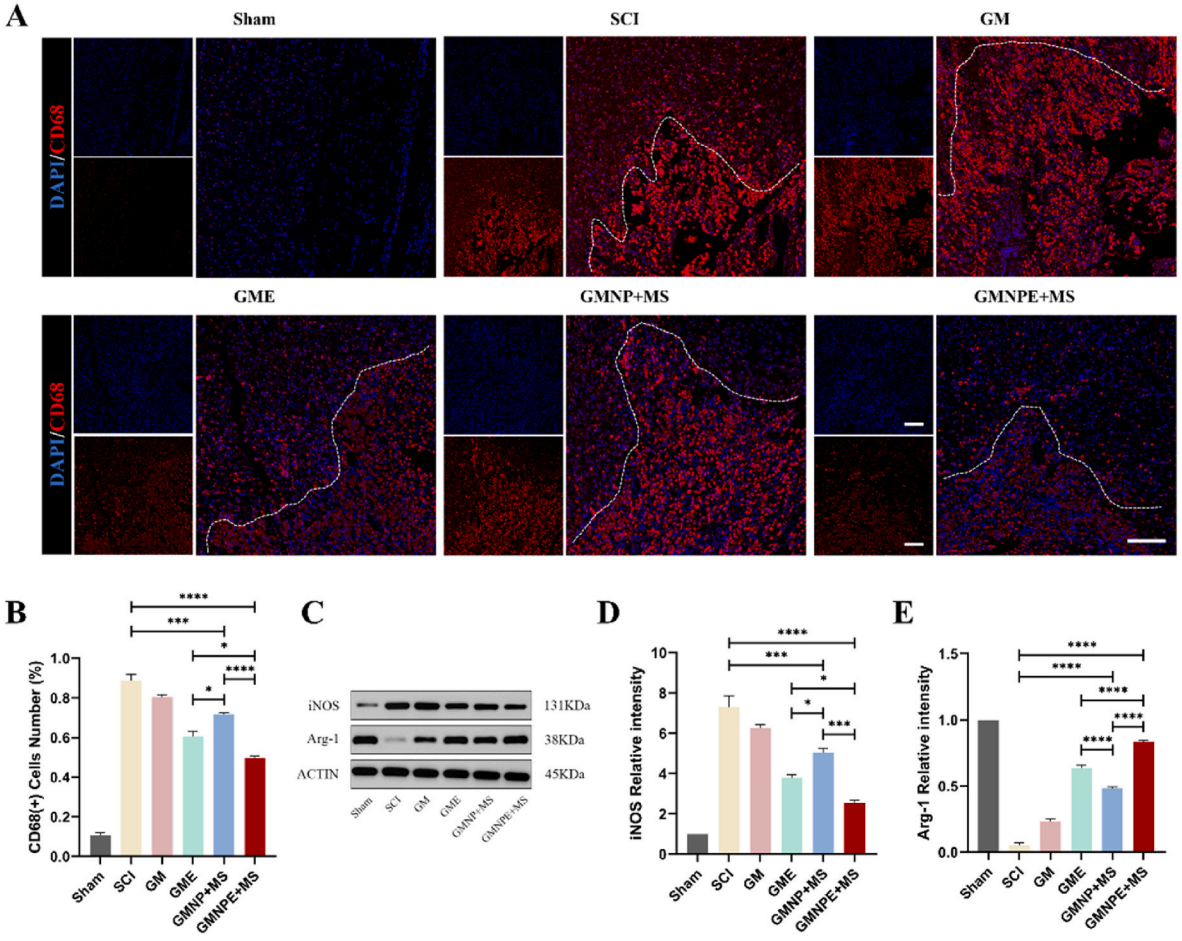

Fig. 7. GMNPE hydrogel inhibited the inflammatory microenvironment in the early stage after SCI. (A) Representative images of immunofluorescence staining of CD68 in each group at day 7 after SCI. Scale bar: 100 μm. (B) Statistical analysis of CD68 (+) cell percentage to total cell number. (n = 3). (C) Western blot image showed the changes in protein expression of iNOS and Arg-1. (D–E) Quantitative analysis of iNOS/ACTIN and Arg-1/ACTIN ratio in western blot images (n = 3). Significance: ns-not significant, *p < 0.05, **p < 0.01, ***p < 0.001, ****p < 0.0001.

minimal CD68(+) immunoreactivity, demonstrating superior combinatorial anti-inflammatory effects through HUMSC-Exos bioactivity and electroconductive modulation (Fig. 7B). WB analyses corroborated these observations: GMNPE + MS group exhibited significantly downregulated iNOS expression alongside upregulated Arg-1 levels compared to SCI, GME, and GMNP + MS groups (Fig. 7C–E). These multimodal findings substantiate that GMNPE hydrogel synergistically leverages exosome-mediated immunomodulation and magnetically triggered electrical cues to suppress early-phase neuroinflammation, thereby mitigating secondary injury cascades and establishing regenerative microenvironments conducive to neural repair.

3.10. GMNPE hydrogel promoted nerve regeneration and axonal regeneration in vivo

To further validate the restorative effect of GMNPE hydrogel on injured spinal cord, we evaluated nerve regeneration at the injury site and glial scar formation by immunofluorescence. Spinal cord tissue was harvested from SCI rats after 8 weeks. Neurons were labeled with Tuj-1 in green and astrocytes were labeled with GFAP in red. Notably, the GMNPE + MS group exhibited substantial accumulation of Tuj-1 (+) neurons within the lesion core, contrasting with the sparse distribution observed in SCI and GM groups (Fig. 8A). Quantitative analysis revealed a significantly higher Tuj-1 (+) area percentage in the GMNPE + MS group (27.9 %) compared to SCI (3.8 %) and GM (8.5 %) groups (Fig. 8B). Conversely, GFAP (+) astrogliosis occupied markedly larger proportions of the lesion area in SCI and GM groups (35.2 % and 28.0 %, respectively) versus GMNPE + MS (9.5 %), with pronounced glial scar formation at lesion peripheries (Fig. 8A and 8C). WB analysis corroborated these findings, showing elevated Tuj-1 expression and reduced GFAP levels in GMNPE + MS versus SCI and GM groups (Fig. 8G–I). To functionally validate neuronal maturation, we quantified axonal regeneration through NF and MBP expression. The GMNPE + MS group demonstrated significantly higher NF (+) axonal density within the

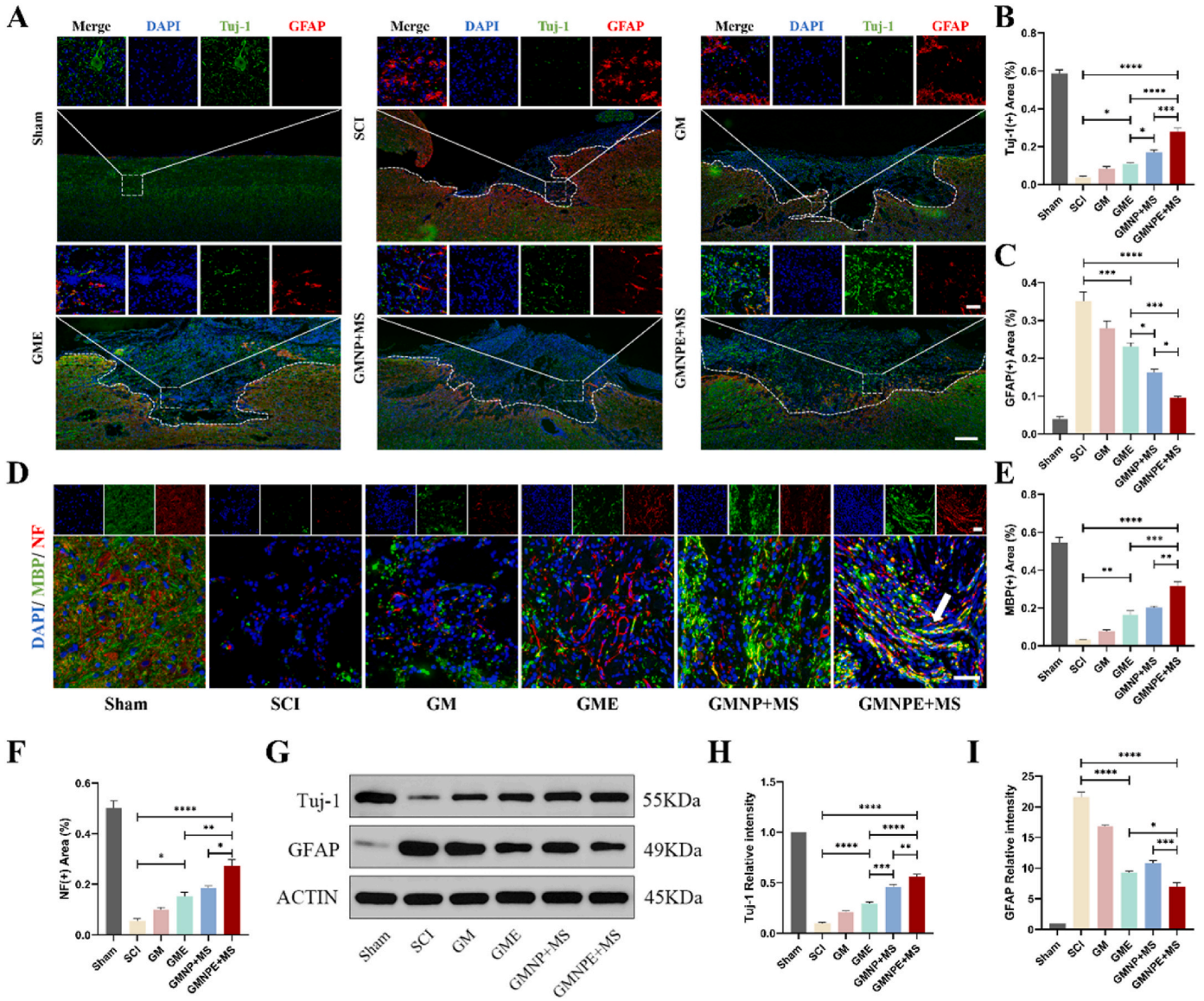

Fig. 8. GMNPE + MS induced differentiation of endogenous NSCs into functional neurons and promoted neuronal regeneration. (A) Representative images of immunofluorescence staining of Tuj-1 (green) and GFAP (red) in each group at week 8 after SCI. Scale bar: 200 μm. Scale bar of magnified image: 50 μm. (B–C) The ratio of Tuj-1 (+) area and GFAP (+) area were quantified (n = 3). (D) Representative images of immunofluorescence staining of MBP (green) and NF (red) in each group at week 8 after SCI. Scale bars: 50 μm. (E–F) The ratio of MBP (+) area and NF (+) area were quantified (n = 3). (G) Western blot image showed the changes in protein expression of Tuj-1 and GFAP. (H–I) Quantitative analysis of Tuj-1/ACTIN and GFAP/ACTIN ratio in western blot images (n = 3). Significance: ns-not significant, *p < 0.05, **p < 0.01, ***p < 0.001, ****p < 0.0001.

lesion epicenter and superior MBP (+) myelination compared to SCI and GM groups (Fig. 8D–F). Moreover, the regenerated axons in the GMNPE + MS group exhibited typical myelin sheath characteristics (indicated by the arrows in Fig. 8D), a feature that was less frequently observed in the other injury groups, excluding the Sham group.

Furthermore, we observed that, compared to the SCI group, both the GME group and the GMNP + MS group exhibited a significant increase in the Tuj-1 (+) area (3.8 % vs. 10.7 % and 17.2 %), along with a significant decrease in the GFAP (+) area (35.2 % vs. 23.2 % and 16.3 %). WB analysis demonstrated a similar trend. These results indicate that the electrical stimulation provided by GMNP + MS and HUMSC-Exos both possess the capability to promote the regeneration of newly formed neurons and reduce glial scar formation. However, the effects of HUMSC-Exos in the GME group were limited and significantly weaker than those provided by electrical stimulation (GMNP + MS). Nevertheless, under the combined influence of both treatments, the GMNPE + MS group exhibited superior neuroregenerative effects, and IF results for NF/MBP further indicated a greater presence of functional neurons in this group.

Collectively, these findings suggest that GMNPE hydrogels, when subjected to magnetic field stimulation, can significantly induce the differentiation of NSCs into functional neurons, promote the regeneration of myelinated nerve fibers, and establish connections between neurons.

4. Discussion

Despite recent advancements in SCI repair research, significant challenges remain. First, the regenerative capacity of nerves after injury is limited, and the microenvironmental changes at the injury site lead to apoptosis of nerve cells and formation of glial scarring, which directly affect the effectiveness of the regeneration process. Furthermore, traditional treatments often fall short in meeting the needs for tissue regeneration and functional recovery, highlighting an urgent demand for new therapeutic approaches. In this context, hydrogel bioscaffolds have emerged as a promising strategy for SCI repair due to their excellent biocompatibility and ability to modulate the local microenvironment. Hydrogels not only mimic the extracellular matrix and provide structural support but also enhance cell adhesion and proliferation by adjusting their physicochemical properties. This capability of hydrogels allows them to improve the local microenvironment, fostering conditions conducive to nerve regeneration. Moreover, their tunable nature enables them to deliver growth factors or drugs locally, promoting nerve function recovery [38–40]. While much of the existing research has focused on the spinal cord structural remodeling, there is a notable gap regarding the impact of the electrical microenvironment on recovery. Electrical stimulation on the spinal cord has been demonstrated to aid functional recovery from injury, suggesting that further exploration in this area could yield valuable insights [17,18].

In this study, we developed a magneto-electric hydrogel with remote noninvasive electrical stimulation function, which can be directly implanted at the SCI site to create an electrical microenvironment at the injury site under the stimulation of a magnetic field, thus promoting nerve repair. The working principle of this magneto-electric hydrogel depends on the fact that when an external magnetic field is applied to Fe_3O_4@$BaTiO_3$ core-shell nanoparticles, the magnetically responsive material undergoes the magnetostrictive effect to produce deformation, which results in mechanical stress on the peripheral piezoelectric material, and according to the piezoelectric effect, the applied stress induces polarization within the piezoelectric material, generating an electric field and thus altering the electrical microenvironment [70]. Previous research supports the efficacy of this approach. Wu et al. demonstrated the biosafety of piezoelectric gels containing $BaTiO_3$ scaffolds for bone regeneration [35]. Similarly, Zhang et al. confirmed the effects of magneto-electric nanoparticles on the proliferation of PC12 cells and the growth of neural synapses [71]. These findings establish a solid foundation for the reliability of our study.

While piezoelectric materials have been extensively explored for osteogenic differentiation and bone regeneration [72,73], their application in SCI therapeutics is relatively scarce. This disparity stems from the inherent biomechanical mismatch between spinal cord tissue and osseous structures—the compliant mechanical properties of neural tissue render conventional piezoelectric systems suboptimal for SCI intervention. The research conducted by Li et al. utilized ultrasound as an external driving source to activate piezoelectric materials for the purpose of generating electrical stimulation in the treatment of SCI [74]. However, the duration of each treatment session cannot be maintained for extended periods, as prolonged ultrasound exposure induces thermal effects that are harmful to nerve regeneration. This limitation highlights the challenges associated with this approach. Some studies have investigated the treatment of SCI through the surgical implantation of piezoelectric stimulators [75]. However, this approach remains limited by the necessity of subsequently removing the electrodes. In contrast, our magnetically driven system enables sustained, non-invasive electrical stimulation through a biodegradable hydrogel platform, obviating recurrent surgery while maintaining therapeutic continuity at the lesion site.

Magnetoelectrically triggered neurostimulation strategies have been previously explored in neural repair applications. For instance, Wang et al. developed slightly flaky graphite nanosheets capable of delivering magnetic field-induced electrical stimulation to enhance neuronal regeneration [23]. However, the immunomodulatory capacity of such materials within the post-SCI inflammatory microenvironment—a critical determinant of neural recovery—remains poorly characterized. In this study, we engineered a synergistic therapeutic platform combining MENPs with HUMSC-Exos, which not only effectively promoted nerve regeneration but also significantly modulated the adverse inflammatory environment post-SCI, demonstrating excellent anti-inflammatory effects. This dual functionality—concurrent neuromodulation and immunoregulation—represents a distinct therapeutic advantage over existing single-modality approaches.

Additionally, our GMNPE hydrogel is composed of gelatin, a degradation product of collagen, combined with methacrylate. This formulation exhibits optimal swelling and mechanical properties that align with the characteristics of neural tissues (0.1–3 kPa), featuring a swelling rate of 777 ± 69 %. These favorable mechanical properties encourage NSCs to differentiate into neurons rather than glial cells [76]. FTIR results confirmed that the incorporation of magneto-electric nanoparticles did not interfere with the hydrogel's bonding structure. Furthermore, prolonged immersion of the GMNPE hydrogel in physiological medium did not result in significant changes in the swelling rate or mechanical properties, indicating long-term stability. Biocompatibility tests, along with in vivo degradation assessments, further validate the biological safety of the GMNPE hydrogel.

SCI triggers the release of numerous cytokines and chemokines, which attracts inflammatory cells to the site, and the activated inflammatory cells not only affect neuronal survival but also inhibit the nerve regeneration process. The HUMSC-Exos incorporated in our GMNPE hydrogel is enriched with a large amount of anti-inflammation-related mRNAs, miRNAs, growth factors, and proteins [45,46]. This property positions HUMSC-Exos as a potential modulator of inflammation. Delivery of immunomodulatory HUMSC-Exos in hydrogels can attenuate adverse host responses and act synergistically with hydrogels to promote functional recovery. Moreover, our in vivo and in vitro experimental results demonstrate that the electrical stimulation provided by MENPs under the influence of a magnetic field also exhibits anti-inflammatory effects, although this effect is weaker than that of HUMSC-Exos [47,77]. Nevertheless, the inflammatory markers in the GMNPE + MS group were significantly reduced compared to both the GME group and the GMNP + MS group, which indicated that the anti-inflammatory effects provided by HUMSC-Exos and the electrical signals work synergistically, leading to the GMNPE + MS group achieving the most remarkable

anti-inflammatory outcome among the injury groups.

In current study, electrical signals were demonstrated to not only promote the differentiation of NSCs into newly formed neurons and oligodendrocytes, but also to inhibit their differentiation into astrocytes, thereby reducing the formation of glial scars. This is consistent with some previous related research findings [23,78]. Furthermore, HUMSC-Exos were also demonstrated in previous reports to possess therapeutic effects in long-term neural regeneration following SCI [60]. This finding was similarly corroborated in our study. It is noteworthy that electrostimulation elicited a significantly greater enhancement in neural regeneration compared to HUMSC-Exos monotherapy, as evidenced by the neurofunctional recovery results of the GMNP + MS group compared to the GME group. Nevertheless, the results from the GMNPE + MS group demonstrate that the combined effects of electrical stimulation and exosomes were significantly superior to either treatment alone.

Our sequencing results identified a significant number of differentially expressed genes associated with several pathways, including neuroactive ligand-receptor interaction, calcium signaling pathway, PI3K-Akt signaling pathway, MAPK signaling pathway, and cAMP signaling pathway, between the GMNPE + MS group and the control group. These pathways are closely related to the differentiation of NSCs and neural regeneration. For instance, the calcium signaling pathway can negatively regulate the PTEN protein, which is a major intrinsic barrier to axon regeneration. Inhibition of PTEN expression allows calcium signaling to promote axon regeneration in corticospinal neurons by upregulating mTOR activity [61,62,79]. The MAPK signaling pathway plays a crucial role in neuronal differentiation, growth, survival, and axon regeneration following central nervous system injury [63]. cAMP signaling is essential for neurite growth and axon guidance, as stimulation of intracellular cAMP activity can significantly enhance neuronal survival and axon regeneration after SCI [64]. Activation of the PI3K-Akt pathway not only promotes the differentiation of NSCs into newly formed neurons and inhibits their differentiation into astrocytes, but also plays a significant role in facilitating neural regeneration and axon growth following injury [47,65–67]. Furthermore, we conducted additional Western blot validation of this pathway, which further suggests that the PI3K-Akt pathway may mediate the process of GMNPE + MS-induced directional differentiation of NSCs and axon regeneration. However, neural differentiation and regeneration are rarely governed by a singular signaling pathway; rather, they constitute a highly orchestrated process involving the interplay of multiple molecular mechanisms. Therefore, further research is needed to explore these molecular mechanisms in greater depth in the future.

Furthermore, although GMNPE + MS has demonstrated significant therapeutic efficacy in SCI repair, substantial challenges must be addressed prior to clinical translation. First, the current surgical implantation protocol for hydrogels risks exacerbating secondary injury. To mitigate this, minimally invasive techniques such as percutaneous injection of thermosensitive hydrogels could be integrated to minimize iatrogenic damage [80]. Second, the static magnetic fields employed in rodent models may not adequately accommodate human anatomical heterogeneity. Developing wearable adaptive magnetic devices equipped with closed-loop feedback systems—capable of dynamically adjusting stimulation intensity based on real-time electrophysiological signals (e.g., EMG/EEG)—could enhance treatment precision in clinical settings [81]. Third, while the degradation kinetics of our hydrogel system align with the axonal regeneration window in rodents, human SCI repair requires sustained structural support over months. Future strategies could involve employing a gradient crosslinking approach to optimize the degradation process of the hydrogel, thereby providing long-term support.

Finally, this study inevitably has some limitations. In future studies, we will further investigate the effects of varying magnetic field strengths and different stimulation durations on the neural functional recovery induced by GMNPE, aiming to identify the optimal stimulation parameters for enhancing neural function recovery. Additionally, we will investigate whether incorporating appropriate conductive materials into the hydrogel influences neurological recovery. Furthermore, more experimental investigations are needed to assess the possible effects of electrical stimulation on HUMSC-Exos. Long-term in vivo studies are also needed to monitor the complete degradation process of our hydrogel over an extended period.

5. Conclusion

In summary, the difficulties in the treatment of SCI not only lie in its complex pathological process, such as post-injury inflammatory response and the difficulty of functional neuron regeneration, but also in the restoration of the electrical microenvironment. We demonstrate that the GMNPE magneto-electric hydrogel, fabricated by integrating Fe_3O_4@$BaTiO_3$ nanoparticles with HUMSC-Exos, enables non-invasive remote electrical stimulation at SCI sites through peripheral magnetic field activation. This innovative system effectively suppresses the inflammatory microenvironment while significantly promoting neuronal survival and axonal regeneration. Among these components, Fe_3O_4@$BaTiO_3$ nanoparticles play a dominant role in nerve regeneration, while HUMSC-Exos are primarily involved in the anti-inflammatory process. The synergistic effect of both components endows the GMNPE hydrogel with excellent anti-inflammatory properties and enhanced neuroregenerative capabilities.

In conclusion, it is crucial that our study offers new insights and directions for future research in the treatment of SCI.

CRediT authorship contribution statement

Wubo Liu: Writing – review & editing, Writing – original draft, Visualization, Validation, Supervision, Software, Resources, Project administration, Methodology, Investigation, Funding acquisition, Formal analysis, Data curation, Conceptualization. **Qiang Liu:** Writing – review & editing, Writing – original draft, Validation, Supervision, Resources, Funding acquisition. **Zeqin Li:** Project administration, Methodology, Investigation, Formal analysis, Data curation. **Chunjia Zhang:** Validation, Supervision, Resources, Project administration, Methodology, Investigation. **Zehui Li:** Project administration, Methodology, Investigation, Data curation, Conceptualization. **Han Ke:** Methodology, Investigation. **Xin Xu:** Methodology, Investigation, Formal analysis. **Xiaoxin Wang:** Software, Resources, Methodology, Investigation. **Huayong Du:** Methodology, Investigation. **Zuliyaer Talifu:** Methodology, Investigation. **Yunzhu Pan:** Methodology, Investigation. **Xiaoxiong Wang:** Validation, Supervision, Methodology, Conceptualization. **Jingyun Mao:** Methodology, Investigation. **Feng Gao:** Visualization, Validation. **Degang Yang:** Validation, Supervision, Methodology. **Yan Yu:** Visualization, Validation, Supervision, Project administration, Methodology, Conceptualization. **Xinyu Liu:** Visualization, Validation, Supervision, Resources, Conceptualization. **Jianjun Li:** Visualization, Validation, Supervision, Resources, Project administration, Funding acquisition.

Ethics approval and consent to participate

The study was approved by the Animal Experimentation Ethics Committee and the Laboratory Animal Welfare Committee of Capital Medical University (AEEI-2022-128) and conducted in accordance with the National Institutes of Health Guide for the Care and Use of Laboratory Animals.

Declaration of competing interest

The authors declare no conflict of interest.

Acknowledgements

The author(s) declare financial support was received for the research, authorship, and/or publication of this article. This research was funded by the Fundamental Research Funds for Central Public Welfare Research Institutes (2022CZ-3), China Rehabilitation Research Center Project (No. 2022ZX-04) and the Special Capital Health Research and Development of China (No. 2018-1-6011). The authors would like to thank the China Rehabilitation Science Institute for providing equipment support and technical assistance for the experiments and thank https://biorender.com for the support of the diagram drawing.

Appendix A. Supplementary data

Supplementary data to this article can be found online at https://doi.org/10.1016/j.bioactmat.2025.02.034.

References

[1] M. Karsy, G. Hawryluk, Modern medical management of spinal cord injury, Curr. Neurol. Neurosci. Rep. 19 (2019) 65.
[2] S.A. Quadri, M. Farooqui, A. Ikram, A. Zafar, M.A. Khan, S.S. Suriya, C.F. Claus, B. Fiani, M. Rahman, A. Ramachandran, I.I.T. Armstrong, M.A. Taqi, M. M. Mortazavi, Recent update on basic mechanisms of spinal cord injury, Neurosurg. Rev. 43 (2020) 425–441.
[3] C. Zhang, Z. Talifu, X. Xu, W. Liu, H. Ke, Y. Pan, Y. Li, F. Bai, Y. Jing, Z. Li, Z. Li, D. Yang, F. Gao, L. Du, J. Li, Y. Yu, MicroRNAs in spinal cord injury: a narrative review, Front. Mol. Neurosci. 16 (2023) 1099256.
[4] T.H. Hutson, S. Di Giovanni, The translational landscape in spinal cord injury: focus on neuroplasticity and regeneration, Nat. Rev. Neurol. 15 (2019) 732–745.
[5] X. Li, Z. Peng, L. Long, Y. Tuo, L. Wang, X. Zhao, W. Le, Y. Wan, Wnt4-modified NSC transplantation promotes functional recovery after spinal cord injury, FASEB J. 34 (2020) 82–94.
[6] X. Du, D. Kong, R. Guo, B. Liu, J. He, J. Zhang, A.E. Amponsah, H. Cui, J. Ma, Combined transplantation of hiPSC-NSC and hMSC ameliorated neuroinflammation and promoted neuroregeneration in acute spinal cord injury, Stem Cell Res. Ther. 15 (2024) 67.
[7] N.A. Silva, N. Sousa, R.L. Reis, A.J. Salgado, From basics to clinical: a comprehensive review on spinal cord injury, Prog. Neurobiol. 114 (2014) 25–57.
[8] D.J. Hellenbrand, C.M. Quinn, Z.J. Piper, C.N. Morehouse, J.A. Fixel, A.S. Hanna, Inflammation after spinal cord injury: a review of the critical timeline of signaling cues and cellular infiltration, J. Neuroinflammation 18 (2021) 284.
[9] L. Ding, W. Chu, Y. Xia, M. Shi, T. Li, F.-Q. Zhou, D.Y.B. Deng, UCHL1 facilitates protein aggregates clearance to enhance neural stem cell activation in spinal cord injury, Cell Death Dis. 14 (2023) 479.
[10] X. Hu, W. Xu, Y. Ren, Z. Wang, X. He, R. Huang, B. Ma, J. Zhao, R. Zhu, L. Cheng, Spinal cord injury: molecular mechanisms and therapeutic interventions, Signal Transduct. Targeted Ther. 8 (2023) 245.
[11] Y. Zheng, Y.-R. Mao, T.-F. Yuan, D.-S. Xu, L.-M. Cheng, Multimodal treatment for spinal cord injury: a sword of neuroregeneration upon neuromodulation, Neural Regen Res 15 (2020) 1437–1450.
[12] B. Yang, F. Zhang, F. Cheng, L. Ying, C. Wang, K. Shi, J. Wang, K. Xia, Z. Gong, X. Huang, C. Yu, F. Li, C. Liang, Q. Chen, Strategies and prospects of effective neural circuits reconstruction after spinal cord injury, Cell Death Dis. 11 (2020) 439.
[13] W.-S. Bang, I. Han, S.-A. Mun, J.-M. Hwang, S.H. Noh, W. Son, D.-C. Cho, B.-J. Kim, C.H. Kim, H. Choi, K.-T. Kim, Electrical stimulation promotes functional recovery after spinal cord injury by activating endogenous spinal cord-derived neural stem/progenitor cell: an in vitro and in vivo study, Spine J. 24 (2024) 534–553.
[14] R. Zhu, Z. Sun, C. Li, S. Ramakrishna, K. Chiu, L. He, Electrical stimulation affects neural stem cell fate and function in vitro, Exp. Neurol. 319 (2019) 112963.
[15] A.F.P. Machado, E.F. Santana, P.M. Tacani, R.E. Liebano, The effects of transcutaneous electrical nerve stimulation on tissue repair: a literature review, Can. J. Plast. Surg. 20 (2012) 237–240.
[16] B. Ferrigno, R. Bordett, N. Duraisamy, J. Moskow, M.R. Arul, S. Rudraiah, S. P. Nukavarapu, A.T. Vella, S.G. Kumbar, Bioactive polymeric materials and electrical stimulation strategies for musculoskeletal tissue repair and regeneration, Bioact. Mater. 5 (2020) 468–485.
[17] C. Marquez-Chin, M.R. Popovic, Functional electrical stimulation therapy for restoration of motor function after spinal cord injury and stroke: a review, Biomed. Eng. Online 19 (2020) 34.
[18] B.A. Karamian, N. Siegel, B. Nourie, M.D. Serruya, R.F. Heary, J.S. Harrop, A. R. Vaccaro, The role of electrical stimulation for rehabilitation and regeneration after spinal cord injury, J. Orthop. Traumatol. 23 (2022) 2.
[19] K.D. Atkins, C.S. Bickel, Effects of functional electrical stimulation on muscle health after spinal cord injury, Curr. Opin. Pharmacol. 60 (2021) 226–231.
[20] M.R. Popovic, T. Keller, I.P. Pappas, V. Dietz, M. Morari, Surface-stimulation technology for grasping and walking neuroprosthesis, IEEE Eng. Med. Biol. Mag. 20 (2001) 82–93.
[21] W.M. Grill, Safety considerations for deep brain stimulation: review and analysis, Expet Rev. Med. Dev. 2 (2005) 409–420.
[22] G. Guízar-Sahagún, I. Grijalva, R.E. Franco-Bourland, I. Madrazo, Aging with spinal cord injury: a narrative review of consequences and challenges, Ageing Res. Rev. 90 (2023) 102020.
[23] L. Wang, H. Zhao, M. Han, H. Yang, M. Lei, W. Wang, K. Li, Y. Li, Y. Sang, T. Xin, H. Liu, J. Qiu, Electromagnetic cellularized patch with wirelessly electrical stimulation for promoting neuronal differentiation and spinal cord injury repair, Adv Sci (Weinh) 11 (2024) e2307527.
[24] P. Chen, C. Xu, P. Wu, K. Liu, F. Chen, Y. Chen, H. Dai, Z. Luo, Wirelessly powered electrical-stimulation based on biodegradable 3D piezoelectric scaffolds promotes the spinal cord injury repair, ACS Nano 16 (2022) 16513–16528.
[25] D.K. Piech, B.C. Johnson, K. Shen, M.M. Ghanbari, K.Y. Li, R.M. Neely, J.E. Kay, J. M. Carmena, M.M. Maharbiz, R. Muller, A wireless millimetre-scale implantable neural stimulator with ultrasonically powered bidirectional communication, Nat. Biomed. Eng. 4 (2020) 207–222.
[26] F. Jin, T. Li, T. Yuan, L. Du, C. Lai, Q. Wu, Y. Zhao, F. Sun, L. Gu, T. Wang, Z.-Q. Feng, Physiologically self-regulated, fully implantable, battery-free system for peripheral nerve restoration, Adv. Mater. 33 (2021) e2104175.
[27] N.A. Kamel, Bio-piezoelectricity: fundamentals and applications in tissue engineering and regenerative medicine, Biophys Rev 14 (2022) 717–733.
[28] N.D. Ferson, A.M. Uhl, J.S. Andrew, Piezoelectric and magnetoelectric scaffolds for tissue regeneration and biomedicine: a review, IEEE Trans. Ultrason. Ferroelectrics Freq. Control 68 (2021) 229–241.
[29] C. Lei, J. Lei, X. Zhang, H. Wang, Y. He, W. Zhang, B. Tong, C. Yang, X. Feng, Heterostructured piezocatalytic nanoparticles with enhanced ultrasound response for efficient repair of infectious bone defects, Acta Biomater. 172 (2023) 343–354.
[30] W. Hiraoka, H. Honda, L.B. Feril, N. Kudo, T. Kondo, Comparison between sonodynamic effect and photodynamic effect with photosensitizers on free radical formation and cell killing, Ultrason. Sonochem. 13 (2006) 535–542.
[31] H. Liu, Y. Shi, Y. Zhu, P. Wu, Z. Deng, Q. Dong, M. Wu, L. Cai, Bioinspired piezoelectric periosteum to augment bone regeneration via synergistic immunomodulation and osteogenesis, ACS Appl. Mater. Interfaces 15 (2023) 12273–12293.
[32] N. Soin, D. Boyer, K. Prashanthi, S. Sharma, A.A. Narasimulu, J. Luo, T.H. Shah, E. Siores, T. Thundat, Exclusive self-aligned β-phase PVDF films with abnormal piezoelectric coefficient prepared via phase inversion, Chem Commun (Camb) 51 (2015) 8257–8260.
[33] A.H. Rajabi, M. Jaffe, T.L. Arinzeh, Piezoelectric materials for tissue regeneration: a review, Acta Biomater. 24 (2015) 12–23.
[34] M. Hoop, X.-Z. Chen, A. Ferrari, F. Mushtaq, G. Ghazaryan, T. Tervoort, D. Poulikakos, B. Nelson, S. Pané, Ultrasound-mediated piezoelectric differentiation of neuron-like PC12 cells on PVDF membranes, Sci. Rep. 7 (2017) 4028.
[35] H. Wu, H. Dong, Z. Tang, Y. Chen, Y. Liu, M. Wang, X. Wei, N. Wang, S. Bao, D. Yu, Z. Wu, Z. Yang, X. Li, Z. Guo, L. Shi, Electrical stimulation of piezoelectric BaTiO3 coated Ti6Al4V scaffolds promotes anti-inflammatory polarization of macrophages and bone repair via MAPK/JNK inhibition and OXPHOS activation, Biomaterials 293 (2023) 121990.
[36] L. Ricotti, A. Cafarelli, C. Manferdini, D. Trucco, L. Vannozzi, E. Gabusi, F. Fontana, P. Dolzani, Y. Saleh, E. Lenzi, M. Columbaro, M. Piazzi, J. Bertacchini, A. Aliperta, M. Cain, M. Gemmi, P. Parlanti, C. Jost, Y. Fedutik, G.D. Nessim, M. Telkhozhayeva, E. Teblum, E. Dumont, C. Delbaldo, G. Codispoti, L. Martini, M. Tschon, M. Fini, G. Lisignoli, Ultrasound stimulation of piezoelectric nanocomposite hydrogels boosts chondrogenic differentiation in vitro, in both a normal and inflammatory milieu, ACS Nano 18 (2024) 2047–2065.
[37] P. Wu, L. Shen, H.-F. Liu, X.-H. Zou, J. Zhao, Y. Huang, Y.-F. Zhu, Z.-Y. Li, C. Xu, L.-H. Luo, Z.-Q. Luo, M.-H. Wu, L. Cai, X.-K. Li, Z.-G. Wang, The marriage of immunomodulatory, angiogenic, and osteogenic capabilities in a piezoelectric hydrogel tissue engineering scaffold for military medicine, Mil Med Res 10 (2023) 35.
[38] B. Guo, P.X. Ma, Conducting polymers for tissue engineering, Biomacromolecules 19 (2018) 1764–1782.
[39] Y. Wu, Y.X. Chen, J. Yan, D. Quinn, P. Dong, S.W. Sawyer, P. Soman, Fabrication of conductive gelatin methacrylate-polyaniline hydrogels, Acta Biomater. 33 (2016) 122–130.
[40] B.M. Baker, C.S. Chen, Deconstructing the third dimension: how 3D culture microenvironments alter cellular cues, J. Cell Sci. 125 (2012) 3015–3024.
[41] L.-S. Wang, J.E. Chung, P.P.-Y. Chan, M. Kurisawa, Injectable biodegradable hydrogels with tunable mechanical properties for the stimulation of neurogenesic differentiation of human mesenchymal stem cells in 3D culture, Biomaterials 31 (2010) 1148–1157.
[42] J.N. Kizhakkedathu, E.M. Conway, Biomaterial and cellular implants: foreign surfaces where immunity and coagulation meet, Blood 139 (2022) 1987–1998.
[43] Y. Zhu, J. Ge, C. Huang, H. Liu, H. Jiang, Application of mesenchymal stem cell therapy for aging frailty: from mechanisms to therapeutics, Theranostics 11 (2021) 5675–5685.
[44] T. Lan, M. Luo, X. Wei, Mesenchymal stem/stromal cells in cancer therapy, J. Hematol. Oncol. 14 (2021) 195.
[45] Y. Yaghoubi, A. Movassaghpour, M. Zamani, M. Talebi, A. Mehdizadeh, M. Yousefi, Human umbilical cord mesenchymal stem cells derived-exosomes in diseases treatment, Life Sci. 233 (2019) 116733.
[46] C.R. Harrell, N. Jovicic, V. Djonov, V. Volarevic, Therapeutic use of mesenchymal stem cell-derived exosomes: from basic science to clinics, Pharmaceutics 12 (2020).
[47] M. Liu, W. Zhang, S. Han, D. Zhang, X. Zhou, X. Guo, H. Chen, H. Wang, L. Jin, S. Feng, Z. Wei, Multifunctional conductive and electrogenic hydrogel repaired

spinal cord injury via immunoregulation and enhancement of neuronal differentiation, Adv. Mater. 36 (2024) e2313672.
[48] W. Man, S. Yang, Z. Cao, J. Lu, X. Kong, X. Sun, L. Zhao, Y. Guo, S. Yao, G. Wang, X. Wang, A multi-modal delivery strategy for spinal cord regeneration using a composite hydrogel presenting biophysical and biochemical cues synergistically, Biomaterials 276 (2021) 120971.
[49] H. Yang, Y. Su, Z. Sun, B. Ma, F. Liu, Y. Kong, C. Sun, B. Li, Y. Sang, S. Wang, G. Li, J. Qiu, C. Liu, Z. Geng, H. Liu, Gold nanostrip array-mediated wireless electrical stimulation for accelerating functional neuronal differentiation, Adv Sci (Weinh) 9 (2022) e2202376.
[50] L.M. Marquardt, V.M. Doulames, A.T. Wang, K. Dubbin, R.A. Suhar, M. J. Kratochvil, Z.A. Medress, G.W. Plant, S.C. Heilshorn, Designer, injectable gels to prevent transplanted Schwann cell loss during spinal cord injury therapy, Sci. Adv. 6 (2020) eaaz1039.
[51] B. Yang, C. Liang, D. Chen, F. Cheng, Y. Zhang, S. Wang, J. Shu, X. Huang, J. Wang, K. Xia, L. Ying, K. Shi, C. Wang, X. Wang, F. Li, Q. Zhao, Q. Chen, A conductive supramolecular hydrogel creates ideal endogenous niches to promote spinal cord injury repair, Bioact. Mater. 15 (2022) 103–119.
[52] T. Vinikoor, G.K. Dzidotor, T.T. Le, Y. Liu, H.-M. Kan, S. Barui, M.T. Chorsi, E. J. Curry, E. Reinhardt, H. Wang, P. Singh, M.A. Merriman, E. D'Orio, J. Park, S. Xiao, J.H. Chapman, F. Lin, C.-S. Truong, S. Prasadh, L. Chuba, S. Killoh, S.-W. Lee, Q. Wu, R.M. Chidambaram, K.W.H. Lo, C.T. Laurencin, T.D. Nguyen, Injectable and biodegradable piezoelectric hydrogel for osteoarthritis treatment, Nat. Commun. 14 (2023) 6257.
[53] A. Saleem, R. Rehman, S. Hussain, M.A. Salem, F. Ali, S.A.A. Shah, U. Younas, S. M. El-Bahy, Z.M. El-Bahy, M. Iqbal, Biodegradable and hemocompatible alginate/okra hydrogel films with promising stability and biological attributes, Int. J. Biol. Macromol. 245 (2023) 125532.
[54] X. Hu, Y. Xu, Z. Zhong, Y. Wu, J. Zhao, Y. Wang, H. Cheng, M. Kong, F. Zhang, Q. Chen, J. Sun, Q. Li, J. Jin, Q. Li, L. Chen, C. Wang, H. Zhan, Y. Fan, Q. Yang, L. Yu, R. Wu, J. Liang, J. Zhu, Y. Wang, Y. Jin, Y. Lin, F. Yang, L. Jia, W. Zhu, J. Chen, H. Yu, J. Zhang, J.a. Wang, A large-scale investigation of hypoxia-preconditioned allogeneic mesenchymal stem cells for myocardial repair in nonhuman primates: paracrine activity without remuscularization, Circ. Res. 118 (2016) 970–983.
[55] M. Prinz, S. Jung, J. Priller, Microglia biology: one century of evolving concepts, Cell 179 (2019) 292–311.
[56] X. Freyermuth-Trujillo, J.J. Segura-Uribe, H. Salgado-Ceballos, C.E. Orozco-Barrios, A. Coyoy-Salgado, Inflammation: a target for treatment in spinal cord injury, Cells 11 (2022).
[57] R. Zhang, W. Mao, L. Niu, W. Bao, Y. Wang, Y. Wang, Y. Zhu, Z. Yang, J. Chen, J. Dong, M. Cai, Z. Yuan, H. Song, G. Li, M. Zhang, N. Xiong, J. Wei, Z. Dong, NSC-derived exosomes enhance therapeutic effects of NSC transplantation on cerebral ischemia in mice, Elife 12 (2023).
[58] M. Revuelta, J. Urrutia, A. Villarroel, O. Casis, Microglia-mediated inflammation and neural stem cell differentiation in alzheimer's disease: possible therapeutic role of KV1.3 channel blockade, Front. Cell. Neurosci. 16 (2022) 868842.
[59] J. Cheng, Z. Chen, C. Liu, M. Zhong, S. Wang, Y. Sun, H. Wen, T. Shu, Bone mesenchymal stem cell-derived exosome-loaded injectable hydrogel for minimally invasive treatment of spinal cord injury, Nanomedicine (Lond) 16 (2021) 1567–1579.
[60] Y. Wang, X. Lai, D. Wu, B. Liu, N. Wang, L. Rong, Umbilical mesenchymal stem cell-derived exosomes facilitate spinal cord functional recovery through the miR-199a-3p/145-5p-mediated NGF/TrkA signaling pathway in rats, Stem Cell Res. Ther. 12 (2021) 117.
[61] Q. Zeng, Z. Zhou, S. Qin, Y. Yao, J. Qin, H. Zhang, R. Zhang, C. Xu, S. Zhang, S. Huang, L. Chen, Rapamycin inhibits B-cell activating factor (BAFF)-stimulated cell proliferation and survival by suppressing Ca2+-CaMKII-dependent PTEN/Akt-Erk1/2 signaling pathway in normal and neoplastic B-lymphoid cells, Cell Calcium 87 (2020) 102171.
[62] Y. Ohtake, U. Hayat, S. Li, PTEN inhibition and axon regeneration and neural repair, Neural Regen Res 10 (2015) 1363–1368.
[63] F.-X. Lin, H.-Y. Gu, W. He, MAPK signaling pathway in spinal cord injury: mechanisms and therapeutic potential, Exp. Neurol. 383 (2025) 115043.
[64] G. Zhou, Z. Wang, S. Han, X. Chen, Z. Li, X. Hu, Y. Li, J. Gao, Multifaceted roles of cAMP signaling in the repair process of spinal cord injury and related combination treatments, Front. Mol. Neurosci. 15 (2022) 808510.
[65] X. He, Y. Li, B. Deng, A. Lin, G. Zhang, M. Ma, Y. Wang, Y. Yang, X. Kang, The PI3K/AKT signalling pathway in inflammation, cell death and glial scar formation after traumatic spinal cord injury: mechanisms and therapeutic opportunities, Cell Prolif. 55 (2022) e13275.
[66] L. Fan, C. Liu, X. Chen, L. Zheng, Y. Zou, H. Wen, P. Guan, F. Lu, Y. Luo, G. Tan, P. Yu, D. Chen, C. Deng, Y. Sun, L. Zhou, C. Ning, Exosomes-loaded electroconductive hydrogel synergistically promotes tissue repair after spinal cord injury via immunoregulation and enhancement of myelinated axon growth, Adv Sci (Weinh) 9 (2022) e2105586.
[67] C. Qin, Z. Qi, S. Pan, P. Xia, W. Kong, B. Sun, H. Du, R. Zhang, L. Zhu, D. Zhou, X. Yang, Advances in conductive hydrogel for spinal cord injury repair and regeneration, Int. J. Nanomed. 18 (2023) 7305–7333.
[68] X. Xu, H.-Y. Du, Z. Talifu, C.-J. Zhang, Z.-H. Li, W.-B. Liu, Y.-X. Liang, X.-L. Xu, J.-M. Zhang, D.-G. Yang, F. Gao, L.-J. Du, Y. Yu, Y.-L. Jing, J.-J. Li, Glycine and N-acetylcysteine (GlyNAC) combined with body weight support treadmill training improved spinal cord and skeletal muscle structure and function in rats with spinal cord injury, Nutrients 15 (2023).
[69] X. Yu, J. Nagai, B.S. Khakh, Improved tools to study astrocytes, Nat. Rev. Neurosci. 21 (2020) 121–138.
[70] S. Kopyl, R. Surmenev, M. Surmeneva, Y. Fetisov, A. Kholkin, Magnetoelectric effect: principles and applications in biology and medicine- a review, Mater Today Bio 12 (2021) 100149.
[71] Y. Zhang, S. Chen, Z. Xiao, X. Liu, C. Wu, K. Wu, A. Liu, D. Wei, J. Sun, L. Zhou, H. Fan, Magnetoelectric nanoparticles incorporated biomimetic matrix for wireless electrical stimulation and nerve regeneration, Adv. Healthcare Mater. 10 (2021) e2100695.
[72] D. Khare, B. Basu, A.K. Dubey, Electrical stimulation and piezoelectric biomaterials for bone tissue engineering applications, Biomaterials 258 (2020) 120280.
[73] C. Yang, J. Ji, Y. Lv, Z. Li, D. Luo, Application of piezoelectric material and devices in bone regeneration, Nanomaterials 12 (2022).
[74] Z. Li, X. Wang, Z. Zhao, Y. Liu, A conductive piezoelectric hydrogel combined with perampanel and wireless electrical stimulation for spinal cord injury repair, Chem. Eng. J. 493 (2024).
[75] S. Li, M. Alam, R.U. Ahmed, H. Zhong, X.-Y. Wang, S. Ng, Y.-P. Zheng, Ultrasound-driven piezoelectric current activates spinal cord neurocircuits and restores locomotion in rats with spinal cord injury, Bioelectron Med 6 (2020) 13.
[76] L. Fan, C. Liu, X. Chen, Y. Zou, Z. Zhou, C. Lin, G. Tan, L. Zhou, C. Ning, Q. Wang, Directing induced pluripotent stem cell derived neural stem cell fate with a three-dimensional biomimetic hydrogel for spinal cord injury repair, ACS Appl. Mater. Interfaces 10 (2018) 17742–17755.
[77] Y. Kong, F. Liu, B. Ma, J. Duan, W. Yuan, Y. Sang, L. Han, S. Wang, H. Liu, Wireless localized electrical stimulation generated by an ultrasound-driven piezoelectric discharge regulates proinflammatory macrophage polarization, Adv Sci (Weinh) 8 (2021) 2100962.
[78] S. Yao, Y. Yang, C. Li, K. Yang, X. Song, C. Li, Z. Cao, H. Zhao, X. Yu, X. Wang, L.-N. Wang, Axon-like aligned conductive CNT/GelMA hydrogel fibers combined with electrical stimulation for spinal cord injury recovery, Bioact. Mater. 35 (2024) 534–548.
[79] K.K. Park, K. Liu, Y. Hu, P.D. Smith, C. Wang, B. Cai, B. Xu, L. Connolly, I. Kramvis, M. Sahin, Z. He, Promoting axon regeneration in the adult CNS by modulation of the PTEN/mTOR pathway, Science 322 (2008) 963–966.
[80] S. Li, C. Yang, J. Li, C. Zhang, L. Zhu, Y. Song, Y. Guo, R. Wang, D. Gan, J. Shi, P. Ma, F. Gao, H. Su, Progress in pluronic F127 derivatives for application in wound healing and repair, Int. J. Nanomed. 18 (2023) 4485–4505.
[81] E. Chen, S. Prakash, V. Janapa Reddi, D. Kim, P. Rajpurkar, A framework for integrating artificial intelligence for clinical care with continuous therapeutic monitoring, Nat. Biomed. Eng. (2023).